9th IAA Planetary Defense Conference – PDC 2025
5–9 May 2025, Stellenbosch, Cape Town, South Africa

IAA-PDC25-0X-YY

Exhaustive search of gravity assist trajectories for rapid reconnaissance and deflection of fictitious asteroid PDC2025

Miguel Gavira-Aladro[a,1,*], Claudio Bombardelli[a,2]

[a] *Universidad Politécnica de Madrid, Plaza Cardenal Cisneros, 28040 Madrid, Spain*

Abstract

The hypothetical asteroid threat exercise for the 2025 Planetary Defense Conference presents an intriguing trajectory design challenge for potential deflection missions. The extended 17-year interval between the impact threat announcement and the possible impact date allows for the exploitation of multiple gravity assist (MGA) trajectories involving inner solar system planets. This enhances the deflection capability of a kinetic impactor and, additionally, facilitates an otherwise very expensive low-relative-velocity rendezvous reconnaissance mission.

In this work, we utilize a rapid, Lambert-free, sequence-independent trajectory-finding algorithm [1], capable of computing all viable MGA trajectories to the asteroid before the expected impact. From these, we select suitable reconnaissance and impact solutions. As anticipated, gravity assists are key in order to achieve a feasible rendezvous without requiring a high-energy launch (C3 $<$ 50 km^2/s^2), with optimal phasing occurring near perihelion. Moreover, some of the most promising trajectories feature multiple resonant legs.

Interestingly, gravity-assist impact trajectories—impacting almost tangentially and near perihelion—appear to be more effective than direct impact trajectories in the proposed scenario. A reconnaissance rendezvous mission followed by a kinetic impact deflection mission is shown to be technologically feasible with carefully designed MGA trajectories, offering multiple launch and arrival opportunities.

Keywords: Reconnaissance mission, asteroid deflection, kinetic impactor, multiple gravity assist

1. Introduction

Following a similar scheme to previous editions ([2], [3]), the 2025 Planetary Defense Conference included a hypothetical asteroid impact scenario to be used as a basis for an emergency response exercise.

The discovery of the fictitious Asteroid 2024 PDC25 is announced on June 6, 2024, and infrared observations by the James Webb Space Telescope confirm its size to be most likely in the 90 to 160 m range and its trajectory to potentially impact the Earth on April 24, 2041, nearly 17 years after the announcement. The impact would occur near the perihelion of the asteroid's orbit and at its ascending node (AN) with a relative velocity of around 8.1 km/s at a roughly 0.9 deg. in-plane angle and 10.7 deg. out-of-plane (ecliptic) angle measured from Earth's velocity vector.

When considering a possible deflection based on a kinetic impact (KI) it is customary to consider two properly coordinated missions: an early reconnaissance mission followed (if needed) by the actual deflection mission. The reconnaissance mission would consist of a space probe performing a rendezvous with the asteroid aimed at characterizing its physical properties and providing an accurate orbital state estimation to confirm or rule out an impact. If an earth impact is confirmed and the asteroid

*Corresponding author
Email address: miguel.gavira.aladro@gmail.com, miguel.gavira.aladro@alumnos.upm.es (Miguel Gavira-Aladro)
[1] Ph.D. Student, Space Dynamics Group
[2] Associate Professor, Space Dynamics Group

characteristics are compatible with a KI deflection the KI mission is launched or, if already launched, finalized. In addition to that, earlier flyby reconnaissance missions with reduced capability compared to a rendezvous mission can also be considered (see [2]). All these missions can, in principle, be designed based on simple direct launch trajectories provided by the solution of Lambert's Problem (LP). However, the orbit characteristics of 2024PDC25 make direct impact and rendezvous trajectories rather challenging with scarce and very narrow launch and arrival windows of opportunity for the impactor, and heavy launcher requirements for the rendezvous spacecraft, as it will be shown in Section 2 of this article. Because a successful deflection mission is imperative in case of a real earth impact threat, having multiple backup opportunities can be crucial for reducing mission risk when facing mission development delays and/or launch delays, thus any amount of flexibility when it comes to departure and arrival windows is highly desirable.

Thanks to a relatively long warning time, and unlike the impact scenarios of previous conferences, it becomes attractive to harness gravity assists with the inner solar system planets to boost the effectiveness of the deflection mission in three main aspects:

1. Potentially increase the achievable KI deflection by allowing a higher relative impact velocity (or reduce launch costs for an equal nominal deflection).
2. Increase the delivered payload mass (or reduce launch costs for equal payload mass delivered) of a reconnaissance mission.
3. Improve the flexibility of the launch window for both the deflection and reconnaissance missions.

As for the first point, a net gain in achievable deflection compared to a direct deflection with no intermediate gravity assists is not obvious as an early kinetic impact benefits from a secularly increasing deflection: one of the objectives of the present analysis is to clarify this aspect. As for the second point, while it is clear that the launch energy for an asteroid rendezvous mission can always be reduced by exploiting gravity assists, the constraint of arriving at the target before the kinetic impactor needs to be carefully taken into account to confirm a clear gain. Last but not least, the possibility of enriching the solution space for candidate reconnaissance-impact trajectory pairs is crucial for planetary defense as it provides multiple mission solutions and backup opportunities.

The main goal of the present work is to fully assess the merits of an MGA-based KI deflection mission compared to a direct transfer approach for both the early reconnaissance and the actual KI deflection trajectory. In order to do that, an exhaustive (STOUR-like, see [4], [5]), flyby-sequence-independent search of all possible, not just optimal MGA ballistic trajectories reaching the asteroid for prescribed Earth launch energy (C_3) and launch date ranges is conducted, exploiting a recently proposed Lambert-free trajectory finding algorithm [1] applied to the specific case of asteroid 2024PDC25. The algorithm is here improved compared to its original version in order to include resonant transfers.

The complete solution space, considering all possible flyby sequences involving the Earth, Venus, Mars and Jupiter and including even and odd-π resonant transfer legs (see [6]), is obtained and post-processed to provide a global picture on the main characteristics of the MGA trajectory design problem. Key aspects including the most promising flyby sequences, the full extent of the MGA-augmented launch window, the improvement of deflection performance, and delivered rendezvous payload mass for reconnaissance, are investigated in detail.

The article is organized as follows. Section 2 gives a detailed definition of the metrics (deflection, payload mass, and arrival relative velocity) used to later compare the solutions obtained. Additionally, it includes a study of the Earth to PDC25 direct transfer problem, with the goal of establishing a well-understood baseline to be compared to the MGA results. Sections 3 and 4 in turn, provide an overview of the MGA problem and its solution using a recently proposed Lambert-free time-matching trajectory finding algorithm [1]. Section 5 covers the theoretical basis for the inclusion of resonant legs in the trajectory finder through the implementation of a resonant chain pathfinder algorithm built on a v_∞-Sphere constraint. Section 6 explores the main pipeline of the sequence-independent exhaustive trajectory finder as a whole and summarizes the search constraints for the results presented in this paper. Finally, Section 7 covers the main results obtained with examples of the best trajectories and Section 8 delves deeper into the characterization of the solution space made possible through the exhaustive nature of the new method.

2. Direct Transfer Baseline Solution

With the aim of comparing the MGA solutions obtained to a well-understood baseline, this section is dedicated to the definition of the metrics and criteria to evaluate the goodness of a particular solution.

The direct transfer problem (i.e. no planetary flybys) can be examined in accordance with these metrics and fundamental insight can be gained to be later applied for the more complex MGA problem.

2.1. Deflection, Payload Mass and Rendezvous Velocity

Arguably the most important metric for a kinetic impactor (KI) mission is its ability to deflect the target, i.e. impart some increment in velocity $\Delta \boldsymbol{V}$ at the time of impact, which gives rise to a small but secularly growing deviation of the asteroid from its predicted path resulting in a near miss at the encounter epoch with the Earth instead of a collision. For the purposes of this work, the deflection effectiveness is quantified through its corresponding B-plane displacement. Many ways exist to compute this quantity ([7], [8], [2]) although for this particular work the authors have chosen to implement a numerical algorithm to determine the increment in b-plane coordinates $\Delta(\Delta \boldsymbol{V}, t_I)$ expressed in Earth radii after the $\Delta \boldsymbol{V}$ is given at the time of impact t_I. Results have been compared and validated with the publicly available NEO Deflection App by NASA/JPL [9].

As for the computation of the deflection impulse $\Delta \boldsymbol{V}$, there is some uncertainty attributed to the additional momentum gained through the dynamics of the cratering process and resulting ejecta [10], which can enhance the momentum transfer through the well-known β-factor ([11],[12]). In this work, however, a conservative approach will be taken in all cases by setting $\beta = 1$ and resulting in the deflection impulse:

$$\Delta \boldsymbol{V} = \frac{m_I}{M} \boldsymbol{v}_\infty \tag{1}$$

Where $M \sim 9.2 \cdot 10^9$ kg is the mass of the asteroid, m_I is the spacecraft mass encountering the asteroid, [3] and $\boldsymbol{v}_\infty$ is the relative asteroid impact velocity.

As for the characterization of a rendezvous reconnaissance mission, the payload mass m_{Pl} that can be slowed down and delivered safely to the vicinity of the asteroid is a fundamental metric. The latter can be computed as:

$$m_{Pl} = m_I \exp\left(-\frac{v_\infty}{I_{sp} g_0}\right) \tag{2}$$

where I_{sp} is the specific impulse of the propulsion system employed to break and rendezvous with the asteroid (here set as 325 s, as achieved with a conventional bipropellant mixture), $g_0 \simeq 9.81 \mathrm{m/s^2}$ and v_∞ is the magnitude of the encounter velocity before the breaking maneuver. Note that the latter is a relevant metric in itself, as lower relative velocities reduce the complexity of the rendezvous process.

2.1.1. Direct Solution Pork-Chop Plots

Figures 1, 2, and 4 illustrate the relevant metrics discussed in this section as functions of the departure date and the time of flight (ToF), obtained using a conventional direct transfer Lambert's Problem solver algorithm [13]. Interesting maxima have been labeled on the plots. Additionally, blue dash-dotted lines have been included to mark the arrival epochs in which PDC25 is at periapsis, and black dashed lines indicate the departure epochs when Earth is closest to the AN of PDC25.

It is clear from Figure 1 that the best chance of deflection comes when impacting the asteroid near its perihelion, to take full advantage of the Oberth effect. The absolute maximum within the region studied corresponds to $\Delta \simeq 2.57$ Earth radii (assuming $\beta = 1$) and would require a departure in early 2026. Due to the scarcity of good solutions, missing this opportunity would cause a deflection loss of more than 0.4 Earth radii and delay the departure to 2027 at the earliest.

As for the rendezvous and reconnaissance mission, Figure 2 shows significant launch C_3 requirements with a considerable increase in mission costs and launcher capabilities. Having said that, there is some more flexibility in terms of departure date and ToF, at least with a launcher similar to or larger than the Falcon Heavy. Even if most local maxima are close to PDC25's periapsis, one can find an interesting apoapsis targeting solution in early 2026 under 500 days of ToF that could be paired with the aforementioned $\Delta \simeq 2.57$ deflection maxima. For this particular scenario, both the reconnaissance and deflection missions would need to depart in early 2026. The reconnaissance vehicle would rendezvous and slow down into a quasi-orbit, with a usable payload of around 2000 kg. Mission control would then have around 300 days of decision time to evaluate the data from the reconnaissance vehicle and target the KI if needed. The two trajectories can be seen in Figure 3.

[3] The mass m_I is determined as a function of the initial $C_{3,0}$ required and the launch vehicle employed, which will be assumed to have a performance similar to that of the Falcon Heavy SpaceX launcher

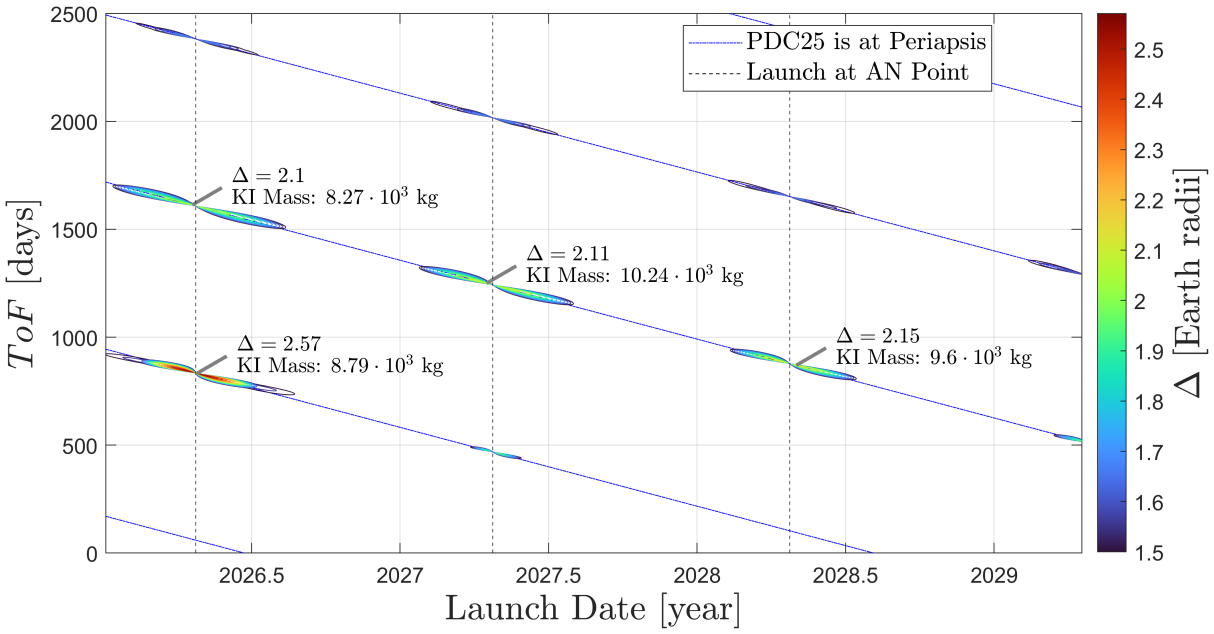

Figure 1: Deflection Conventional PCP.

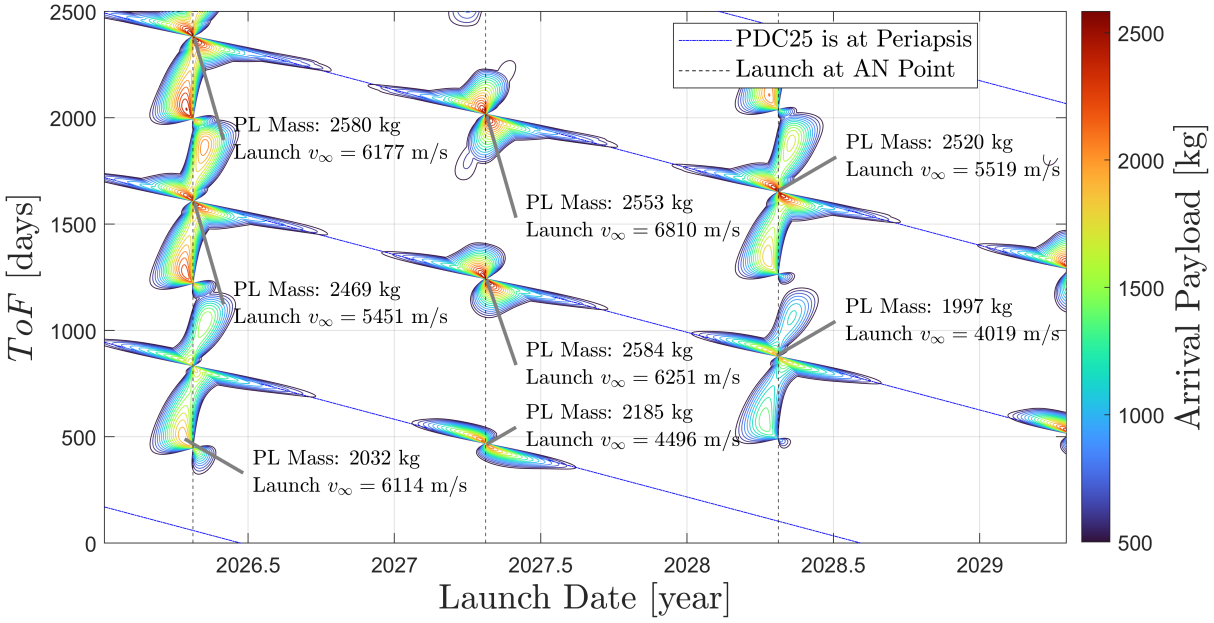

Figure 2: Payload Mass Conventional PCP.

Finally, Figure 4 shows that it is possible to reach PDC25 with an extremely small relative velocity, provided a very large initial $C_3 \sim 70\text{km}^2/\text{s}^2$ is attainable by the launcher and one is not concerned about the maximum time of flight (ToF). Note that for most local optima in Figures 2 and 4 departure dates and times of flight coincide, but the trajectory required for optimum payload mass does not minimize arrival velocity as well (the corresponding launch v_∞ values differ considerably). This is due to a complex tradeoff between the launch and arrival maneuvers where launching at the highest possible velocity is not the most efficient strategy for achieving the largest possible payload mass.

In summary, the analysis of the direct transfer solution in this section clarifies that with a launcher similar to the Falcon Heavy:

1. A deflection of $\Delta \simeq 2.57$ Earth radii can be achieved if arrival in 2028 is possible.
2. After a considerable braking maneuver at the rendezvous epoch, around 2500 kg of usable payload can be delivered.
3. Very low rendezvous velocities can be achieved but at large launch costs ($C_3 > 60\ \text{km}^2/\text{s}^2$).

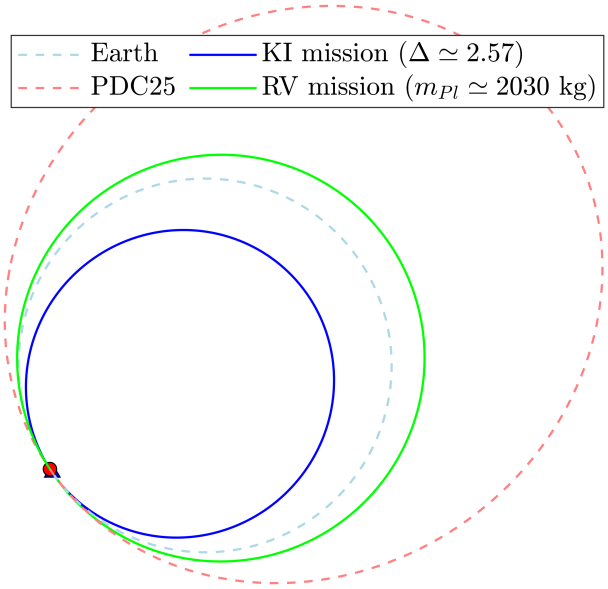

Figure 3: Best rendezvous + deflection solutions. Departing Earth on Apr 26 2026. KI mass is approximately 8800 kg.

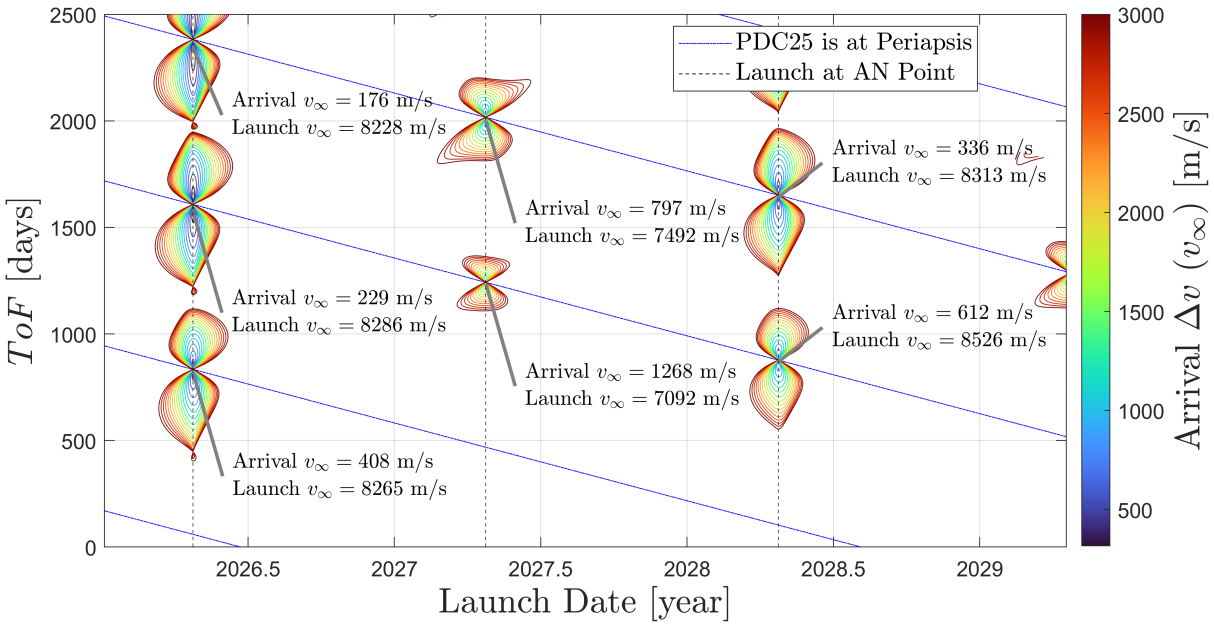

Figure 4: Rendezvous v_∞ Conventional PCP.

4. For deflection purposes, only two viable impact opportunities exist: late 2028 and late 2030.

3. Multiple Gravity Assist Problem Solution Count

A key aspect motivating the choice of an exhaustive method instead of a traditional or heuristic optimization approach [14] is the finite number of possible ballistic MGA trajectories once a launch date t_0, initial energy $v_{\infty,0}$ and maximum ToF are specified. This property can be demonstrated as follows:

For a single-leg transfer departing from a planet P_0 to a planet P_1 with a fixed departure date t_0 and launch $v_{\infty,0}$, all possible trajectories are discrete in terms of arrival time as a fundamental characteristic of Lambert's Problem. In other words, when one takes a fixed $v_{\infty,0}$ and fixed t_0 slice of a Pork-Chop plot, one obtains individual points (transfer trajectories) each one characterized by its ToF value. The number of points grows depending on the maximum allowed ToF but remains finite. Now consider adding another planet (P_2) to the sequence. Because ballistic gravity assists preserve relative velocity,

time and energy conditions at P_1 departure (t_1,$v_{\infty,1}$) are fixed and, through the same reasoning as before, the number of solutions arriving at P_2 now including a gravity assist at P_1 is still finite.

However, it is important to keep in mind that even if finite, the number of possible $P_0 \rightarrow P_1 \rightarrow P_2$ trajectories might quickly escalate if the transfer time limit is chosen laxly. This is because adding a gravity assist to the chain fundamentally amounts to a branching of the solution tree even if it does not add any more degrees of freedom to the problem(see Figure 5). Provided the very first conditions (t_0 and $v_{\infty,0}$) are fixed, the number of solutions is still finite, even if large; [5] or [1] feature some examples of tree examples similar to Figure 5.

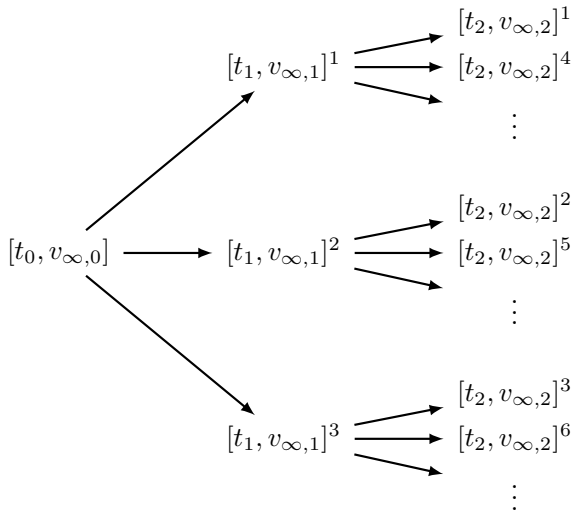

Figure 5: Branching of the solutions due to a gravity assist at P_1.

Including resonant legs does result in more degrees of freedom in the solution space and requires special attention. Fortunately, resonant transfers can be omitted from the calculation of the main (non-resonant) sequence and instead treated as "gap fillers" which fix the phasing of an otherwise impossible non-resonant sequence. In the end, the discrete nature of the solution for any given initial condition still holds. The fact that given initial conditions the number of paths to the target under a given total flight time restriction is limited allows for the definition of "exhaustive" trajectory finding methods, aimed at obtaining the complete solution space for some grid of initial conditions, and not just individual local optima. The full characterization allows for a straightforward determination of the best possible solution in terms of initial energy, total time of flight or other criteria, as well as having direct access to all kinds of Pareto front solutions of interest. Lastly, large scale data analysis can be performed on the solution set to study different features of the MGA solution space.

4. Lambert-free Time Compatibility Method

Classical exhaustive methods like STOUR ([4], [5]) include a Lambert-based algorithm known as C_3-matching, where the C_3 constant for a generic transfer leg i can be obtained as:

$$C_{3,i} = v_{\infty,i}^2 = (\boldsymbol{v}_i^{out} - \boldsymbol{v}_i^P)^2 = (\boldsymbol{v}_i^{in} - \boldsymbol{v}_i^P)^2 \tag{3}$$

Where $\boldsymbol{v}_i^{in(out)}$ is the heliocentric velocity of the vehicle before(after) the assist and $\boldsymbol{v}_i^P$ is the planet's velocity at the assist epoch t_i. For each $P_i \rightarrow P_j$ transfer, solutions are found by computing the necessary $C'_{3,i}$ to arrive at the target at candidate epoch t'_j through solving Lambert's Problem. This function $C'_{3,i}(t'_j; \dots)$ which not only depends on t'_j is matched with the true initial energy condition of that particular transfer $C_{3,i} = v_{\infty,i}^2$. Those t_j epochs where the values meet make up the transfer solution set, $\boldsymbol{t}_j$.

While this algorithm is conceptually simple, it can be demanding in terms of computation time, which motivated the development of an alternative scheme where it is the arrival epoch t_j which is matched instead of the departure energy $C_{3,i}$. The idea behind this new "time-matching" method is described in detail in [1] and has some key computational advantages. In Figure 6 both algorithms are compared at a conceptual level. Additionally, it includes a few more relevant transfer parameters to be defined:

- N, the number of S/C full revolutions during the transfer leg,
- Δt_R, a time offset to keep track of the phasing gaps to be filled with resonance chains (to be defined later),
- and and integer index λ or α depending on the matching algorithm to keep track of the particular Lambert's Problem solution or Compatibility Quartic solution.

For the energy-matching, one needs to choose a particular solution of Lambert's Problem, by picking a direction: prograde or retrograde, and an arc type: short or long way. $\lambda = 1, 2, 3, 4$ keeps track of the four possibilities. In much the same way, when matching time, one needs to choose one out of the four possible quartic solutions, $\alpha = 1, 2, 3, 4$ keeps track of that. Finally, the vector $\boldsymbol{t}_j$ contains the set of valid arrival epochs.

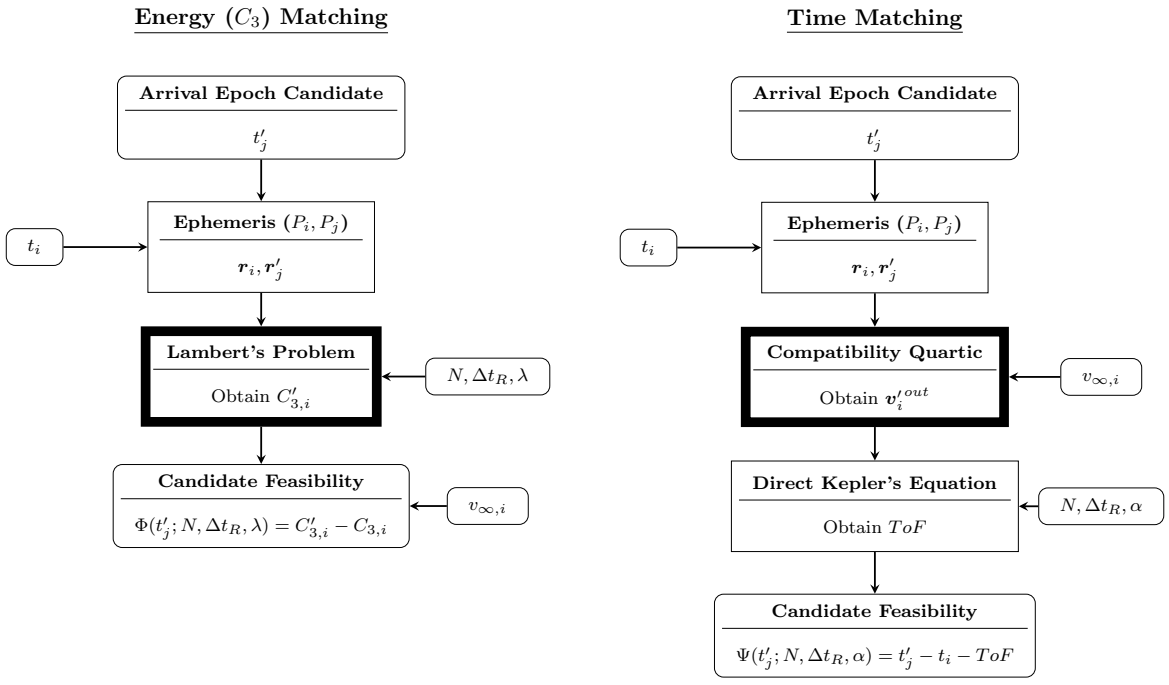

(a) Energy-matching **(b) Time-matching**

Figure 6

The computational bottleneck of each algorithm is indicated with a thicker border block. While both methods are similar in concept, there are two clear advantages to the time-matching proposed in [1]:

1. Lambert's Problem requires by nature an iterative algorithm which adds complexity, and needs to be called once per λ value. The Compatibility Quartic can be solved analytically in a more direct way, or converted to an eigenvalue extraction problem and solved numerically through any of the well known methods. Either way, all four solutions are found at once and in parallel.
2. When time-matching, the computationally costly step is independent of most parameters, as N and Δt_R appear only in Kepler's Equation meaning the bulk of the computation does not need to be repeated if many values of N and Δt_R are to be considered.

To further elaborate on the second point, consider the following expression, (Eq. 27 of [1]) where an additional term $-\Delta t_R$ is added to account for time lost due to possible resonant chains before the departure from P_i:

$$\Psi(t_j; N, \Delta t_R, \alpha) = t_j - t_i - \Delta t_R - \left(\sqrt{\frac{a_\alpha^3}{\mu_\odot}} (\Delta E_\alpha - \sin \Delta E_\alpha + 2\pi N) + \frac{r_i r_j}{\sqrt{\mu_\odot p_\alpha}} \sin \Delta\theta_\alpha \right) \tag{4}$$

$\Delta E, \Delta\theta$ represent the increments in eccentric and true anomaly associated with the transfer leg, and a, p are the semimajor axis and the semilatus rectum of the outgoing transfer arc. As there are 4 solutions to the Compatibility Quartic, the subindex α denotes those variables which depend on the quartic solution index. $\mu_\odot$ is the standard gravitational parameter of the Sun.

It is clear from (4) that the dependency on N and Δt_R is explicit and easy to treat. This happens due to the fact that the v_∞-Sphere constraint is being applied first and the time-matching, which is the part where most of the parameters become relevant, is left as the last step, as seen in Figure 6. When C_3 matching, however, the time constraint is considered first, and the v_∞-Sphere last, thus the parameter dependency has to be included in the bulkiest part of the calculation.

This fact becomes relevant when searching for zeros, as the first step involves the discretization of a t'_j interval, and computation of $\Psi(\Phi)$ when time(energy)-matching, for a range values and several parameter combinations of N, Δt_R, and $\alpha(\lambda)$. It is strongly beneficial to use Ψ, where the dependency on the parameters is very shallow and the bulkiest part of the computation can be easily reused. Additionally, the more cumbersome part involves only a quartic equation, instead of an implicit LP solver.

A quick comparison of both matching algorithms can be seen in Figure 7. Where instead of Φ, the alternative

$$\hat{\phi} = \sqrt{C'_{3,i}} - \sqrt{C_{3,i}} \tag{5}$$

has been plotted for ease of comparison reasons. The four viable solutions, illustrated in Figure 8, that is, the four possible transfers for departure date and energy with $N = 0$ or $N = 1$ have been plotted. Due to the multiplicity of solutions of both the Compatibility Quartic (α), and Lambert's Problem (λ), Ψ and $\hat{\Phi}$ are multi-valued functions. Due to its simpler "loop" morphology, finding the zeros of Ψ can be easier than doing the same on $\hat{\Phi}$, which as can be seen in Figure 7, is defined for larger t'_j intervals meaning a larger region to scan for zeros.

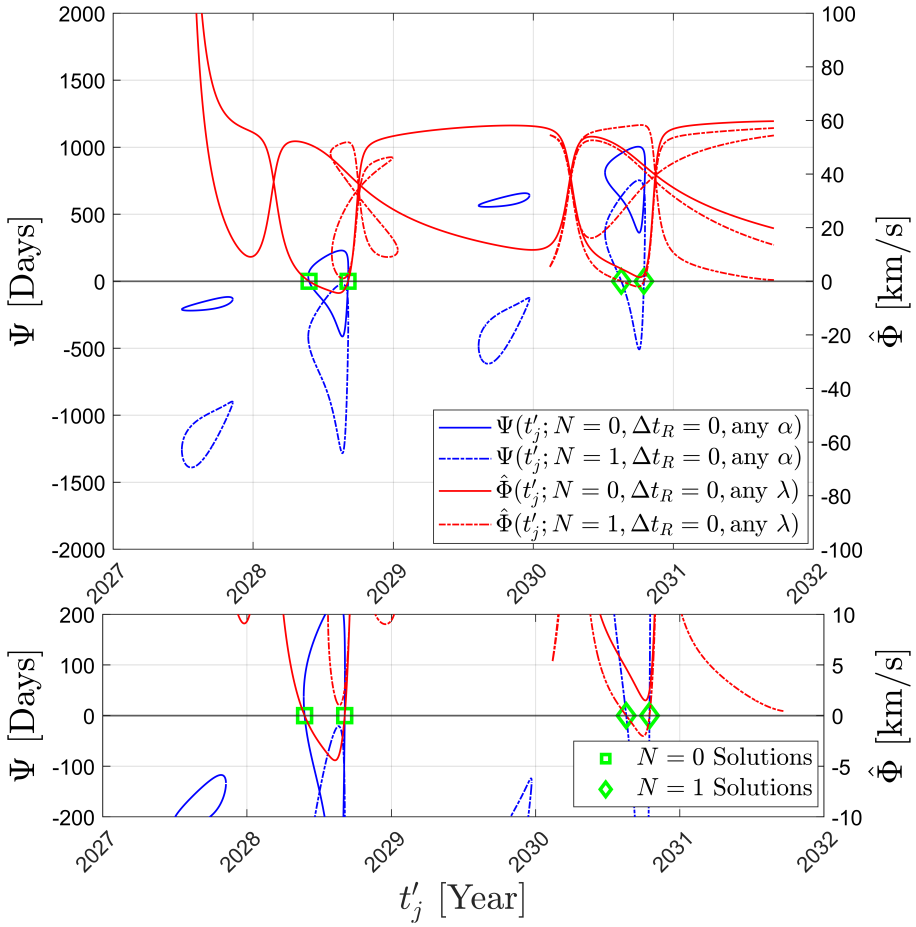

Figure 7: Energy vs. Time-matching algorithms. Earth to PDC25 departing on Jun 25 2027 with $C_3 = 55\text{km}^2/\text{s}^2$.

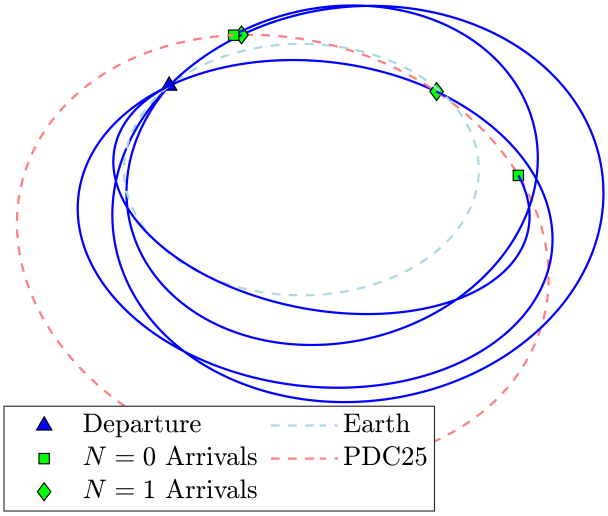

Figure 8: Matched solutions from Figure 7. Departing Earth on Jun 25 2027 with $C_3 = 55\text{km}^2/\text{s}^2$.

Regardless of the algorithm, however, once the "matched" transfers are found, the incoming and outgoing relative velocities need to be computed:

$$\boldsymbol{v}_{\infty,i}^{in} = \boldsymbol{v}_i^{in} - \boldsymbol{v}_i^P \tag{6}$$

$$\boldsymbol{v}_{\infty,i}^{out} = \boldsymbol{v}_i^{out} - \boldsymbol{v}_i^P \tag{7}$$

and the viability of the deflection must be assessed. The deflection limit the assisting body P_i can provide δ_i^{max} is obtained from the minimum allowable periapsis radius $r_{p,i}^{min}$ and standard gravitational parameter.

$$\delta_i^{max} = \pi - 2\cos^{-1}\left(\frac{1}{1 + \frac{r_{p,i}^{min} v_{i,\infty}^2}{\mu_i}}\right) \tag{8}$$

Only if the actual deflection δ_i required is smaller than the maximum, that particular time/energy-matched solution can be considered valid:

$$\cos^{-1}\left(\frac{\boldsymbol{v}_{i,\infty}^{in} \cdot \boldsymbol{v}_{i,\infty}^{out}}{v_{i,\infty}^2}\right) = \delta_i < \delta_i^{max} \tag{9}$$

5. Including Resonant Transfers

The original time-matching and sequence-independent trajectory finder developed in [1] lacked the ability to include resonant legs, which can be conveniently classified into two types depending on the transfer angle θ:

1. $\theta = 2n\pi \quad n \in \mathbb{N}^+$ or complete, even resonances, and
2. $\theta = (2n-1)\pi \quad n \in \mathbb{N}^+$ or half way, odd resonances.

"Even-π" resonances are more common and can be considered in either matching algorithm as time gaps [6] in the assist sequence to be filled. Including a $2n\pi$ leg is analogous to delaying the final departure by a time equal to an integer number of periods T_i of the assisting planet M_i, thus amounting to a simple offset of Ψ, through the parameter $\Delta t_R = M_i T_i$. In addition, the assist deflection constraint needs to be modified to account for the additional deflections the gap-filling resonant chain can provide, which might make feasible an otherwise impossible deflection, by splitting it into smaller steps. This requires solving a pathfinding problem on the v_∞-Sphere where the $\boldsymbol{v}_\infty$ vector starts at $\boldsymbol{v}_\infty^{in}$ and jumps from one resonant arc to the next one in the chain until eventually reaching $\boldsymbol{v}_\infty^{out}$, as will be shown later in this section.

"Odd-π" resonances are considerably less common, becoming very rare if the target P_j is a different planet from the assisting P_i. These $(2n-1)\pi$ cases can be treated like normal transfers, with the only particularity being that some terms of the Compatibility Quartic become singular for $\theta = (2n-1)\pi$, i.e. the v_∞-Sphere constraint does not provide enough information to solve the problem if $\theta = (2n-1)\pi$, and an auxiliary implicit algorithm is required.

5.1. Even (Type 1) Resonance Chains

Consider a $2n\pi$ leg amounting to a transfer compatibility offset $\Delta t_R = M_i T_i$ equivalent to M_i periods of the assisting planet P_i. In order to fill the gap, a set of resonant legs is flown, each of these characterized by the resonant ratio:

$$R_k = \frac{N^k}{M_i^k} \tag{10}$$

where $N^k(M_i^k) \in \mathbb{N}^+$ is the minimum number of vehicle(planet) revolutions until the next encounter. The following restriction applies to the complete sequence:

1. The total time of flight of the resonance sequence must equal the known time-matching gap $\Delta t_R = M_i T_i$, thus,
$$\sum_k M_i^k = M_i \tag{11}$$
2. All deflections required must verify the single assist deflection constraint from Eq. (8) for planet P_i.
$$\delta_t^{t+1} < \delta_i^{max} \tag{12}$$

Another index t is introduced to keep track of the actual positions of the $\boldsymbol{v}_\infty$ vector, starting with $\boldsymbol{v}_{\infty,i}^{in}$ then moving through all the $\boldsymbol{v}_{\infty,i}^{k}$ that each leg k in the resonant chain requires, and finally to $\boldsymbol{v}_{\infty,i}^{out}$. For instance, a resonant chain involving two legs, $k \in [1,2]$, would have $t \in [in, 1, 2, out]$ and requires three $\boldsymbol{v}_\infty$ jumps: $in \to 1$, $1 \to 2$, and $2 \to out$, which independently need to fulfill (12). There can be an infinite amount of valid resonant chains according to Eqs. (11) and (12), but crucially, choosing a particular solution over another does not affect the rest of the sequence, as the actual $P_i \to P_j$ transfer has already been determined through the time-matching algorithm. Including a $2n\pi$ sequence is just a way to fill a phasing gap in the transfer, but otherwise the main transfer sequence is completely ignorant of the particular gap filler solution. Arrival conditions to planet P_j are the same regardless.

Considering this fact, the goal of this section is not to provide means for the characterization of the complete solution space of resonant chains fulfilling the constraints in Eqs. (11) and (12), which might be really large. But rather to prove the chain's feasibility and find a single particular solution.

5.1.1. Parametrization of the v_∞-Sphere

The final relative velocity a gravity assist can provide is fully determined by two parameters, as it is constrained to the surface known as the v_∞-Sphere. To arrive at a useful parametrization of this surface, consider the following unit vectors,

$$\boldsymbol{u}_v = \frac{\boldsymbol{v}_i^P}{v_i^P} \tag{13}$$

$$\boldsymbol{u}_h = \frac{\boldsymbol{r_i} \times \boldsymbol{v}_i^P}{|\boldsymbol{r} \times \boldsymbol{v}_i^P|} \tag{14}$$

$$\boldsymbol{u}_n = \boldsymbol{u}_h \times \boldsymbol{u}_v \tag{15}$$

In addition, consider two angles $\xi \in [0, \pi]$, and $\eta \in [0, 2\pi]$ as illustrated in Figure 9, and obtained from:

$$\cos\xi = \boldsymbol{u}_\infty \cdot \boldsymbol{u}_v \tag{16}$$

$$\sin\eta \sin\xi = \boldsymbol{u}_\infty \cdot \boldsymbol{u}_h \tag{17}$$

$$\cos\eta \sin\xi = \boldsymbol{u}_\infty \cdot \boldsymbol{u}_n \tag{18}$$

where $\boldsymbol{u}_\infty = \boldsymbol{v}_\infty / v_\infty$.

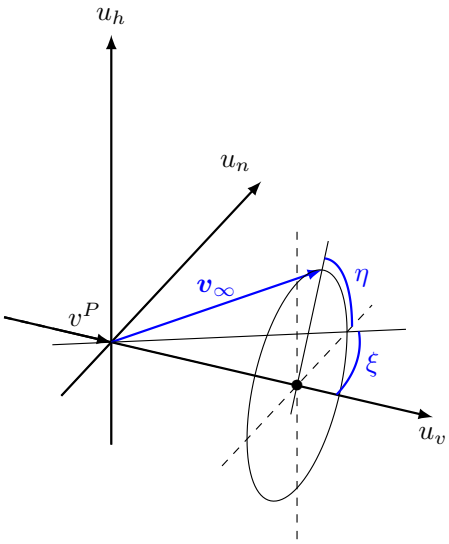

Figure 9: Definition of the parametrization angles ξ and η for the v_∞-Sphere.

The ratio between the magnitudes of the outgoing heliocentric velocity of the vehicle $v_{i,k}^{out}$ at the k-th leg of the chain and the planet's own velocity v_i^P can be written in terms of ξ_k:

$$\left(\frac{v_{i,k}^{out}}{v_i^P}\right)^2 = 1 + \left(\frac{v_{\infty,i}}{v_i^P}\right)^2 + 2\frac{v_{\infty,i}}{v_i^P}\cos\xi_k = 1 + A^2 + 2A\cos\xi_k \tag{19}$$

Where the parameter $A = v_{\infty,i}/v_i^P$ is introduced. The resonant ratio R_k can be computed as:

$$R_k = \left(\frac{a_i^P}{a_i^{out}}\right)^{3/2} = \left(\frac{\dfrac{2\mu_\odot}{r_i v_i^{P2}} - \left(\dfrac{v_{i,k}^{out}}{v_i^P}\right)^2}{\dfrac{2\mu_\odot}{r_i v_i^{P2}} - 1}\right)^{3/2} = \left(\frac{B - \left(\dfrac{v_{i,k}^{out}}{v_i^P}\right)^2}{B-1}\right)^{3/2} \tag{20}$$

With $B = 2\mu_\odot/r_i v_i^{P2}$. The substitution of Eq. (19) into Eq. (20) leaves R_k as a function exclusively involving the particular pathfinding problem parameters (A, B) and ξ_k, completely independent of η_k:

$$R_k = \begin{cases} \left[1 - \dfrac{A^2 + 2A\cos\xi_k}{B-1}\right]^{3/2}, & \text{if} \quad \dfrac{A^2 + 2A\cos\xi_k}{B-1} < 1, \\ 0, & \text{otherwise.} \end{cases} \tag{21}$$

$R_k = 0$ stands for those values of ξ_k for which the outgoing trajectory becomes hyperbolic. In general, $R_k \in [R_k^{min}, R_k^{max}]$, an interval which in turn depends on the limit values for ξ_k. If no additional constraints are considered, and in the interest of generality $\xi_k \in [0, \pi]$ for all legs,

$$R_k^{min} = \begin{cases} \left[1 - \dfrac{A^2 + 2A}{B-1}\right]^{3/2}, & \text{if} \quad \dfrac{A^2 + 2A}{B-1} < 1, \\ 0, & \text{otherwise.} \end{cases} \tag{22}$$

$$R_k^{max} = \begin{cases} \left[1 - \dfrac{A^2 - 2A}{B-1}\right]^{3/2}, & \text{if} \quad \dfrac{A^2 - 2A}{B-1} < 1, \\ 0, & \text{otherwise.} \end{cases} \tag{23}$$

5.1.2. Finding the possible resonant chains

In the last section, a clear relation has been established between the resonance ratio of each outgoing leg R_k and the parametrization angles of the v_∞-Sphere, particularly ξ_k. For a particular pathfinding problem, however, not all values of $R_k = N^k/M_i^k$ are interesting; only those that can construct a valid resonance chain should be considered.

From the constraint in Eq. (11), it is clear that $M_i^k \leq M_i$. Additionally, considering R_k^{min} and R_k^{max},

$$\text{foreach} \quad M_i^k \Rightarrow N^k \in \left[n^k \in \mathbb{N}^+ \middle| \lceil M_i^k R_k^{min} \rceil \leq n^k \leq \lfloor M_i^k R_k^{max} \rfloor \right] \tag{24}$$

Which is to say that N^k can only take values that guarantee $R_k \in [R_k^{min}, R_k^{max}]$. Then, once all possible R_k candidates have been obtained, they need to be arranged in every possible combination fulfilling the constraint in Eq. (11). Finally, each combination can be evaluated to check for violations of maximum deflection Eq. (12).

Consider the following example where the assisting body P_i is the Earth ($B \sim 2$) and a rather large $v_\infty \simeq 10$ km/s, meaning $A \sim 1/3$. Under these circumstances, $R_k^{min} \simeq 0.105$ and $R_k^{max} \simeq 1.940$ for all k if $\xi_k \in [0, \pi]$ is allowed. Additionally, consider that the time gap to be covered by the chain is 3 years long, thus $M_i = 3$ and thus $M_i^k \in [1, 2, 3]$. Applying Eq (24) gives the following ratios:

$$R^k = N^k : M_i^k \in \{1:1 \ / \ 1:2 \ / \ 3:2 \ / \ 1:3 \ / \ 2:3 \ / \ 4:3 \ / \ 5:3\}$$

Figure 10 illustrates the fixed ξ_k arcs corresponding to the ratios above.

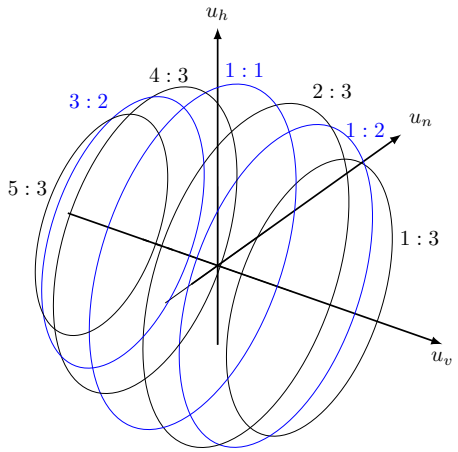

Figure 10: Resonant arcs available for chain construction with $B = 2, A = 1/3, M_i = 3$.

Keeping only the unique values of R^k, there are therefore seven possible puzzle pieces which one might use to solve the pathfinding problem. The last four, for which $M_i^k = M_i = 3$ fulfill (11) by themselves. Those for which $M_i^k = 2$ need to be combined with one $M_i^k = 1$ leg. The final alternative is to have 3 consecutive $M_i^k = 1$ legs to cover the gap. The set of possible chains valid under Eq (11) is therefore:

$$\left\{ \begin{array}{ccc} 1:1 \rightarrow 1:1 \rightarrow 1:1 & 1:1 \rightarrow 1:2 & 1:1 \rightarrow 3:2 \\ 1:2 \rightarrow 1:1 & 3:2 \rightarrow 1:1 & 1:3 \\ 2:3 & 4:3 & 5:3 \end{array} \right\}$$

Reciprocal chains such as $1:1 \rightarrow 1:2$ and $1:2 \rightarrow 1:1$ need to be checked separately, since the feasibility of each chain also depends on whether or not the first arc, ($1:1$ or $1:2$) can be reached from the entrance point $v_{\infty,i}^{in}$. The same holds for $v_{\infty,i}^{out}$, for the chain to be valid, it must be reachable with a deflection under δ_{max} from the last arc.

5.1.3. Checking the feasibility of a resonance chain

Once the set of possible chains has been determined, all that is left is to check for the feasibility of each one. As mentioned previously, the goal of this section is not finding every possible path but rather determining whether valid paths exist. With that mindset, once one viable solution is found for a particular chain, the others need not be checked. Figure 11 illustrates two paths for the aforementioned example. The $1:2 \rightarrow 1:1$ path in Figure 11a involves little deflections and ends up being valid, while the $1:1 \rightarrow 1:1 \rightarrow 1:1$ path in Figure 11b requires a very large initial deflection to get from $\boldsymbol{v}_{\infty,i}^{in}$ to $\boldsymbol{v}_{\infty,i}^{k=1}$ in the the $1:1$ arc, and thus should be discarded.

To compute the feasibility of a path between $\boldsymbol{v}_{\infty,i}^{in}$ and $\boldsymbol{v}_{\infty,i}^{out}$, which requires getting from some coordinates ξ_{in}, η_{in} to ξ_{out}, η_{out}, through a set of intermediate points $\xi_1, \eta_1; \xi_2, \eta_2; \ldots$, the deflection of each jump needs to be computed using the haversine formula:

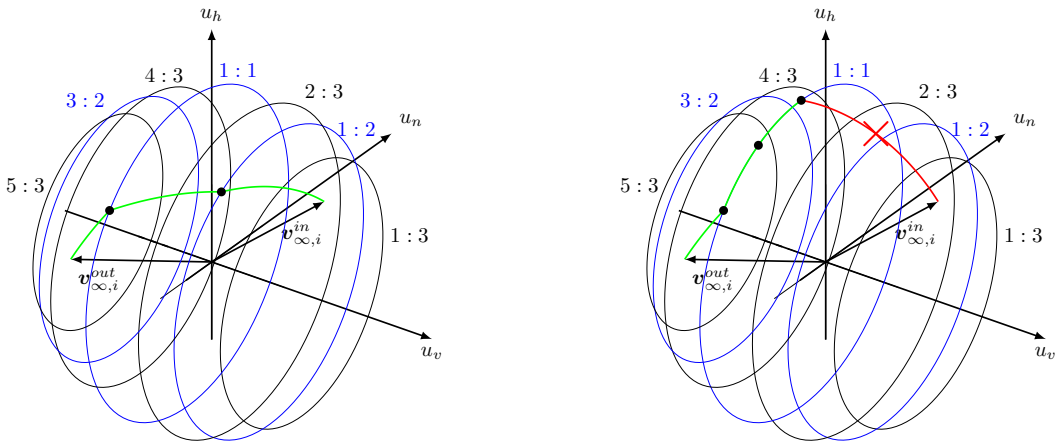

(a) Valid $1:2 \rightarrow 1:1$ **path.** **(b) Invalid** $1:1 \rightarrow 1:1 \rightarrow 1:1$ **path.**

Figure 11: Different $M_i = 3$ **paths on the** v_∞**-Sphere, with** $B = 2, A = 1/3$**.**

$$\cos\delta_t^{t+1} = \cos\xi_t \cos\xi_{t+1} + \sin\xi_t \sin\xi_{t+1} \cos(\Delta_t^{t+1}\eta). \tag{25}$$

Where $\Delta_t^{t+1}\eta$ is the increment in η of each jump, and as mentioned previously $t \equiv in, 1, 2, \ldots, out$. If any particular $|\xi_{t+1}$ - $\xi_t|$ is larger than δ_{max}, that chain candidate can be discarded right away. If however all ξ jumps are feasible, then the next key step is to compute the total increment in η that particular chain would provide, if all deflections were strained to the δ_{max} limit. In this way, if the "η budget" that could be achieved by always deflecting $\boldsymbol{v}_\infty$ the maximum available at each step on the chain is larger than what is needed to cover the gap between η_{out} and η_{in} which is always smaller than π, then the chain must be feasible. Introducing $\delta = \delta_{max}$ in Eq. (25) and solving for $\Delta_t^{t+1}\eta$.

$$(\Delta_t^{t+1}\eta)_{max} = \cos^{-1}\left[\max\left(-1, \frac{\cos\delta_{max} - \cos\xi_t\cos\xi_{t+1}}{\sin\xi_t \sin\xi_{t+1}}\right)\right]. \tag{26}$$

Finally, considering the above, a sufficient condition for the chain to be feasible would be

$$(\Delta_{in}^{out}\eta)_{max} > \Delta_{in}^{out}\eta \longrightarrow \sum_{t=in}^{out-1} (\Delta_t^{t+1}\eta)_{max} > \Delta_{in}^{out}\eta \tag{27}$$

Where $\Delta_{in}^{out}\eta = \min(|\eta_{out} - \eta_{in}|, 2\pi - |\eta_{out} - \eta_{in}|)$. To recap, the set of steps to determine whether or not a particular $\Delta_R t$ gap can be filled with a resonant sequence is the following:

1. From the time gap, determine M_i, and the pathfinding problem parameters $A = v_{\infty,i}/v_i^P, B = 2\mu_\odot/r_i v_i^{P2}$.
2. Get the set of reachable resonant arcs R_k.
3. Get all the possible chains adding up to M_i that can be constructed using those resonant arcs.
4. Evaluate the feasibility of each chain until one is found to be valid, or all can be discarded.
5. If at least one valid solution has been found, continue solving the MGA sequence.

5.2. Odd (Type 2) Transfers

The underlying reason behind the necessity of a particularized treatment for $\theta = (2n-1)\pi$ transfers is the indetermination of the trajectory plane. Fixing the candidate arrival epoch $t'_j = t^*_j$ so that $\theta = (2n-1)\pi$, is not enough to collapse the matching function Ψ or Φ to a finite set of values. As can be seen in Figure 7, this is not true in a general case. When t'_j is fixed at some arbitrary epoch, $\Psi(\Phi)$ depends only on the integer parameters $N, \alpha(\lambda)$ or on quantities that can only take discrete values $(\Delta_R t)$.

However, in the particular case $t'_j = t^*_j$, $\Psi(\Phi)$ can still take a whole continuous range of values because the trajectory plane is undefined. To keep track of its orientation, a new dependency in $\Psi(\Phi)$ appears, which can be mapped to a new parameter τ. There are many ways to define this new parameter, and depending on whether one is energy-matching (Φ) or time-matching (Ψ), some definitions are more convenient than others. For this work, and only in these particular $\theta = (2n-1)\pi$ cases, the authors have chosen to go with the energy alternative; thus, τ has been defined as:

$$\tau = \text{atan2}\Big(\boldsymbol{v}_i^{out} \cdot (\boldsymbol{u}_h \times \boldsymbol{u}_r), \boldsymbol{v}_i^{out} \cdot \boldsymbol{u}_h\Big) \tag{28}$$

Where $\boldsymbol{u}_r = \boldsymbol{r}_i / r_i$. u_h has been previously defined in Eq. (14). The particular algorithm implemented involves first assuming $\tau = 0$, i.e. the trajectory plane being perpendicular to that of P_i, the assisting planet, and then solving Lambert's Problem to get an outgoing velocity $\boldsymbol{v}_i^{out}$ in that perpendicular plane. The obtained outgoing velocity candidate could be rotated by any angle τ around $\boldsymbol{u}_r$ and still provide a trajectory reaching r'_j. However, only a finite set of τ values end up resulting in $\boldsymbol{v}_i^{out}$ being on the v_∞-Sphere. An implicit zero-finding algorithm is used to determine the values of τ complying with this requisite. Since τ is a relatively simple parameter, the computation time is small when compared to everything else.

It should be noted that, even when the target P_j is the same as the assisting planet P_i, the critical epoch $t'_j = t^*_j$ when $\theta = (2n-1)\pi$ might not exist, as planetary trajectories are not strictly Keplerian, nor does the orbital plane remain constant in time. Thus in general there is no t'_j at which r'_j is exactly collinear with r_i. However, epochs when $\theta = (2n-1)\pi \pm \varepsilon$ where $\varepsilon \sim 10^{-4}$ are close enough to cause numerical instabilities in the matching algorithms. Thus, implementation-wise, the authors have chosen to exclude these small time ranges (~ 1 day) from the conventional time-matching zero search. The solutions that would appear in these small intervals are substituted by approximations assuming $\theta = (2n-1)\pi \pm \varepsilon \simeq (2n-1)\pi$. The resulting targeting errors in these approximated transfers under the collinear simplification are negligible, in the order of 10^2km.

Other than that, these solutions are treated the same as every other, and added to the set of possible initial conditions to the next transfer.

6. The Sequence-Independent MGA Trajectory Finder

The concepts described in the previous sections have been utilized by the authors to construct a new sequence-independent ballistic MGA trajectory finder tool which exhaustively examines a grid of initial conditions to find all paths reaching a particular target, PDC25 in this case. The objective of this approach is to provide a holistic view of the solution space rather than focusing on individually good or Pareto-optimal solutions. Having access to the complete MGA solution space for a large grid of departure dates and energies not only provides globally optimum solutions in terms of selected objective functions (deflection Δ, payload mass m_{Pl}, or rendezvous velocity v_∞), but also greatly simplifies the analysis of the launch windows and identification of backup alternatives.

Additionally, introducing gravity assists is expected to greatly enrich the solution space compared to a direct transfer strategy (Figures 1, 2, and 4). Producing full MGA pork-chop plots, comparing them to the direct-transfer ones, and evaluating how gravity assists transform the solution space is another key feature of the present tool.

6.1. Algorithm description

Figure 12 aims to summarize the behavior of the sequence-independent MGA ballistic trajectory finder algorithm employed to obtain the results presented in this work. The branching nature of the solution structure (as seen in Figure 5) motivates an iterative core algorithm that keeps track of the length of the current sequence. For this purpose, a new integer index χ is introduced, accompanied by a variable size data structure $\mathcal{I}_\chi$ which keeps track of the continuation points from which to generate new transfers to the multiple celestial bodies available. Thus, in the context of a complete MGA solution involving multiple legs, the so far generic indices i, j in $P_i \rightarrow P_j$ will be replaced with $\chi, \chi+1$, as in $P_\chi \rightarrow P_{\chi+1}$, situating the particular transfer within the sequence.

The algorithm starts at level $\chi = 0$ taking a single initial condition from the grid: $[t_0, \boldsymbol{v}_{\infty,0}]$ and adds it to a set of possible continuation points at that level $\mathcal{I}_0$. For $\chi = 0$, $\mathcal{I}_0$ only contains the initial condition of the problem, but for larger χ, $\mathcal{I}_\chi$ might contain multiple possible initial conditions ($[t_\chi, \boldsymbol{v}_{\infty,\chi}]^\ell$) due to the branching, where the index ℓ is used to identify each one.

Then, for each continuation point ℓ, the solver iterates through all possible targets (for this work: Earth, Venus, Mars, Jupiter, and PDC25) using another index $m = 1, 2, \ldots, 5$, and finds all possible transfers to each of them. As there may be multiple solutions, yet another index q is required. Thus,

- for level χ (length of the sequence so far),
- ℓ keeps track of continuation points from which to generate new transfers,

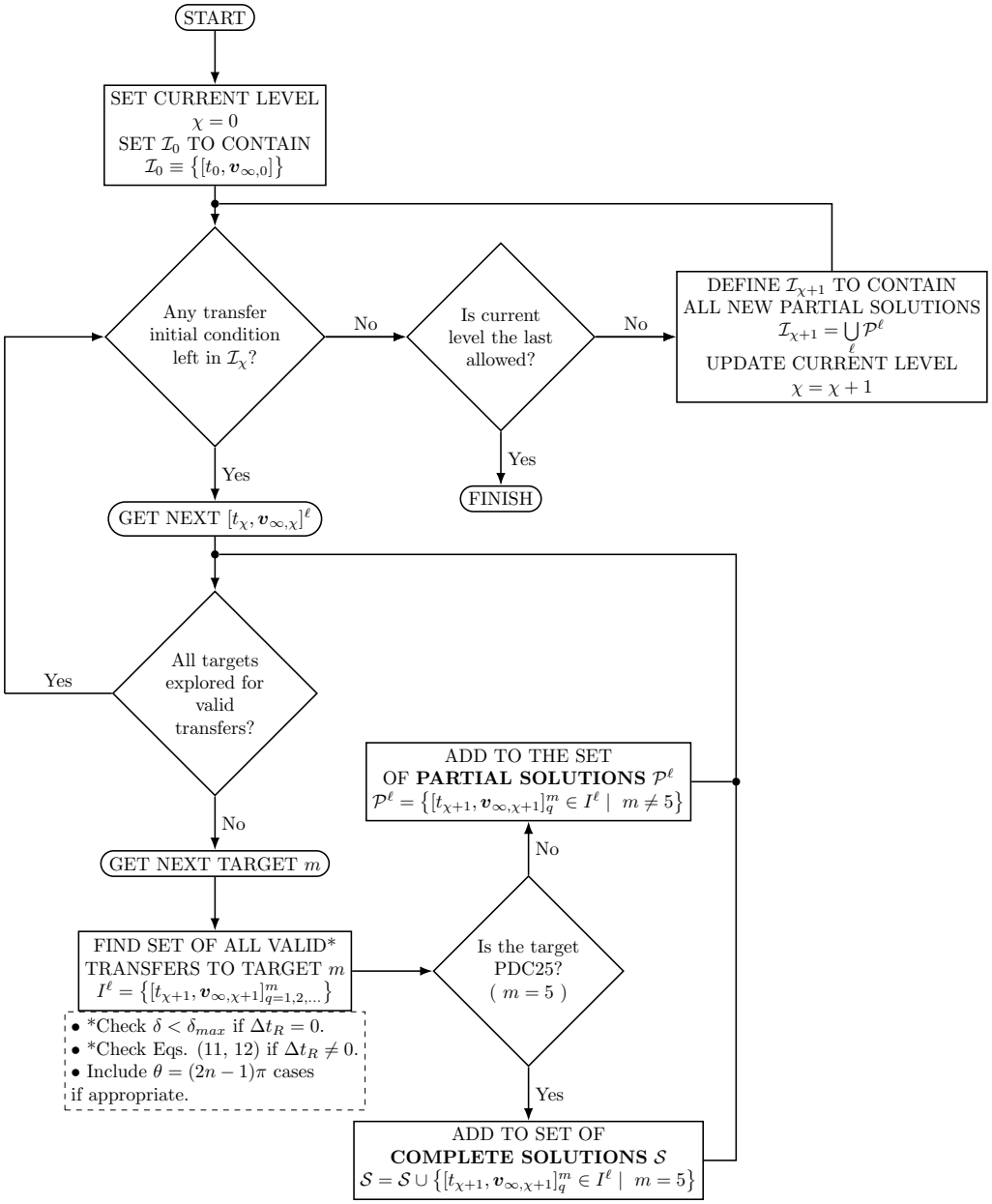

Figure 12: Flow chart of the sequence independent trajectory finder

- m identifies the transfers generated to a particular body,
- and q identifies a particular transfer solution in the set corresponding to an ℓ, m pair.

Once all m have been explored for all ℓ, finding all possible transfers to all the possible targets, those aimed at PDC25 ($m = 5$) need to go no further, already completing particular solutions, and can be added to a set $\mathcal{S}$ containing all of the complete sequences so far. On the contrary, if the target m is not PDC25, and there are still levels available ($\chi < \chi^{max}$), these transfers are appended to the preceding sequence leading to $[t_\chi, \boldsymbol{v}_{\infty,\chi}]^\ell$ and become, if deflection constraints are met, a set of partial sequences $\mathcal{P}^\ell$ to be possibly completed by legs in later levels. Lastly, those not meeting deflection or resonance constraints are discarded. When all continuation points (ℓ) at that level (χ) have been explored, all unfinished sequences in the $\mathcal{P}^\ell$ sets are combined together to form the set of continuation points for the next level $\mathcal{I}_{\chi+1}$.

It should be noted that even if t_χ and $\boldsymbol{v}_{\infty_\chi}$ for all χ are enough to identify a particular solution of the MGA problem, and everything else can be computed from them, the program stores significantly more information about each sequence as χ increases and it grows in length, for data analysis and plotting purposes.

- Number of complete revolutions of each transfer N_χ,
- deflection required at each flyby δ_χ,
- detailed information (ξ_k, η_k, R_k) of the resonant chains if $\Delta t_R \neq 0$ for any of the transfers,
- and heliocentric velocities before and after flybys.

When χ has reached its maximum allowed for all paths or a level has been reached for which the set of continuations is empty, $\mathcal{I}_\chi \equiv \emptyset$, the initial condition $[t_0, \boldsymbol{v}_{\infty,0}]$ is considered exhausted, and the program moves to a new one until everyone in the initial condition grid is fully exhausted.

6.2. Search parameters and constraints for trajectories to PDC25

Table 1 describes the main parameters of the grid search conducted; in particular, the earliest departure date has been set to be in January 2026 assuming a minimum lead time of around 1.5 years from the initial discovery until the reconnaissance and deflection missions can be launched. The rest of the parameters have been chosen by trial and error after exploring the solution space with small-scale tests to ensure good coverage of the interesting area of the solution space in the main run of the program while keeping the solution number manageable.

Table 1: Grid search parameters and their values.

Grid Parameter	Value
Earliest Departure Epoch	*Jan-04-2026 12:00 (TDB)*
Latest Departure Epoch	*Apr-21-2029 00:00 (TDB)*
Grid Spacing (Departure Epoch)	2.5 days
Minimum Departure Energy	$v_{\infty,0}^{min} = 2$ km/s
Maximum Departure Energy	$v_{\infty,0}^{max} = 5$ km/s
Grid Spacing (Departure Energy)	50 m/s
Grid Size	482×61

Table 2 covers the constraints for the trajectory finder, these have been set as laxly as possible to get the best view of the solution space while lowering the actual number of solutions per initial condition to be at most around $1 \cdot 10^5$. Particularly, a stricter time limit is applied to Earth → Earth and Venus → Venus transfers. They can provide time delays to fix phasing gaps relative to PDC25, but barely, if at all, increase the relative velocity and are prone to filling up the solution space. On the contrary, trajectories involving Jupiter are expected to be a rare but interesting possibility, and the limits for transfers to or from Jupiter have been relaxed. Finally, the maximum duration of the last leg to PDC25 is also less tightly constrained to make sure no good solution is lost. Importantly, the exhaustive nature of the method makes imposing further restrictions very easy once the solution space is completely known by simply filtering the results.

Table 2: Grid search constraints and their values.

Constraint	Value
Latest Allowed Arrival Epoch	*17-Dec-2036 12:00 (TDB)*
Maximum Number of Flybys	$\chi^{max} = 5$ (Resonance chains only count as 1 flyby)
Allowed Assisting Planets	Venus (V), Earth (E), Mars (M), Jupiter (J)
Minimum Flyby Altitudes	V - 300 km, E - 300 km, M - 200 km, J - 630000 km
Maximum Duration of Transfer	by default: 850 days if Jupiter is involved: 1200 days if PDC25 is involved: 1000 days if Earth → Earth : 560 days if Venus → Venus : 350 days

7. Deflection, Rendezvous and reconnaissance via MGA

Solving every single grid point according to Figure 12 resulted in a solution set $\mathcal{S}$ containing 552 million individual trajectories reaching PDC25 with 249 possible combinations of flyby sequences (leaving out sequences differing only by resonant legs). This section is dedicated to a brief discussion of the main results and the best trajectories for the rendezvous (RV) and kinetic impactor (KI) missions, while Section 8 will contain more detailed information on the characteristics of the solution space as a whole, including the effectiveness of the different sequences found at providing solid trajectories for a potential KI mission and the importance of each assisting planet on the solution space.

7.1. Multiplanetary Pork-Chop plots

Figure 13 shows a scatter plot where every trajectory with a deflection over $\Delta = 1.5$ Earth radii (42 million, $\sim 7.61\%$ of the entire solution space $\mathcal{S}$) has been plotted according to the time of departure, the total time of flight, and the achieved asteroid deflection at the impact epoch in 2041. This representation is similar to a classic PCP, and can be compared directly to the equivalent PCP for the direct transfer in Figure 1.

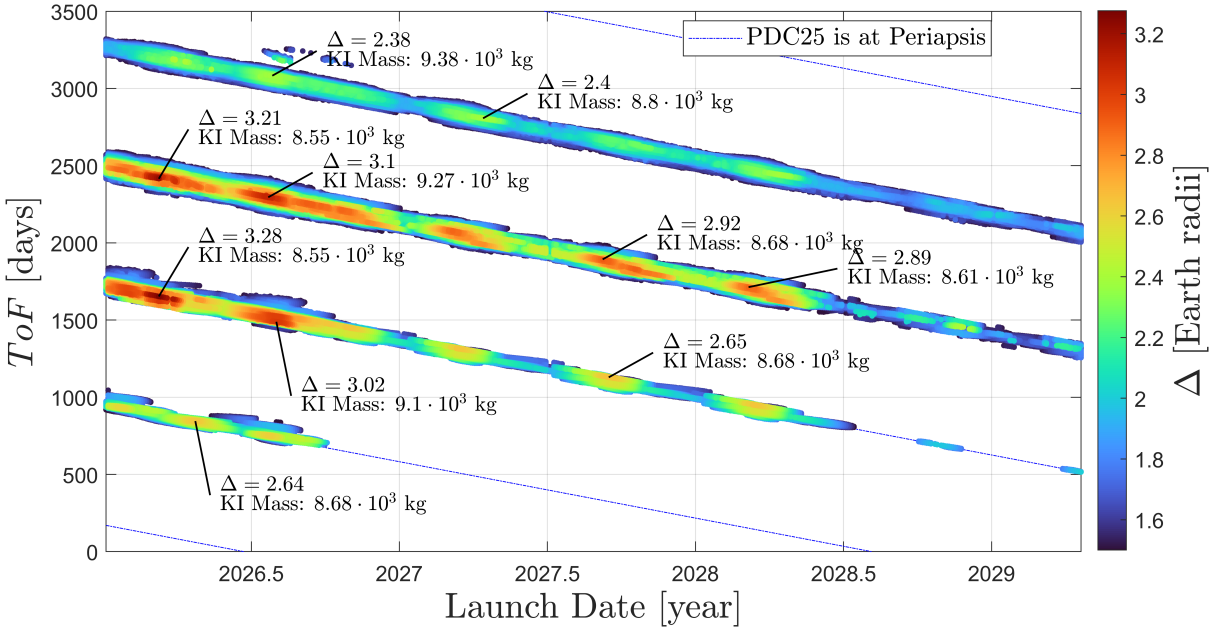

Figure 13: MGA Sequence Independent Deflection PCP.

Several interesting local maxima have been labeled according to the deflection they provide and the mass of the KI if launched with a vehicle with a performance similar to that of the Falcon Heavy in fully expendable mode. Notably, while Figure 1 showed that launching at the epoch when the Earth is close to the AN of PDC25 is an effective strategy, this is no longer the case when gravity assists are involved. On the contrary, similarly to the direct-transfer solution in Figure 1 most good solutions still arrive when PDC25 is at its perihelion, due to the Oberth effect. The only exception is a set of Jupiter trajectories departing in late 2026, with a $ToF \sim 3200$ days, clearly impacting outside the main periapsis lines.

The highest deflection in the solution space is achieved by a 5-flyby-long "VEVEV" trajectory (Figure 16a) with no resonant legs departing in early 2026 and impacting during 2030, resulting in a deflection of $\Delta \simeq 3.28$, a 27% improvement with respect to the best possible direct transfer from Figure 1, which demonstrates that the 17 years between the discovery of 2024 PDC25 and the potential impact in 2041 provide enough time to take advantage of gravity assists. The increase in impact velocity this strategy provides outweighs the shorter secular propagation of the deflection.

Similarly, Figure 14 shows every trajectory able to put more than 500 kg on a quasi orbit around PDC25. The very considerable reduction in launch C_3 made possible through the use of gravity assists to accelerate the reconnaissance vehicles and match the orbit of PDC25 results in much larger payload capacity. If one can afford long trip times, up to 6000 kg can be delivered (Figure 16b) before the periapsis crossing in late 2032, more than doubling what could be done with a direct transfer (Figure 2).

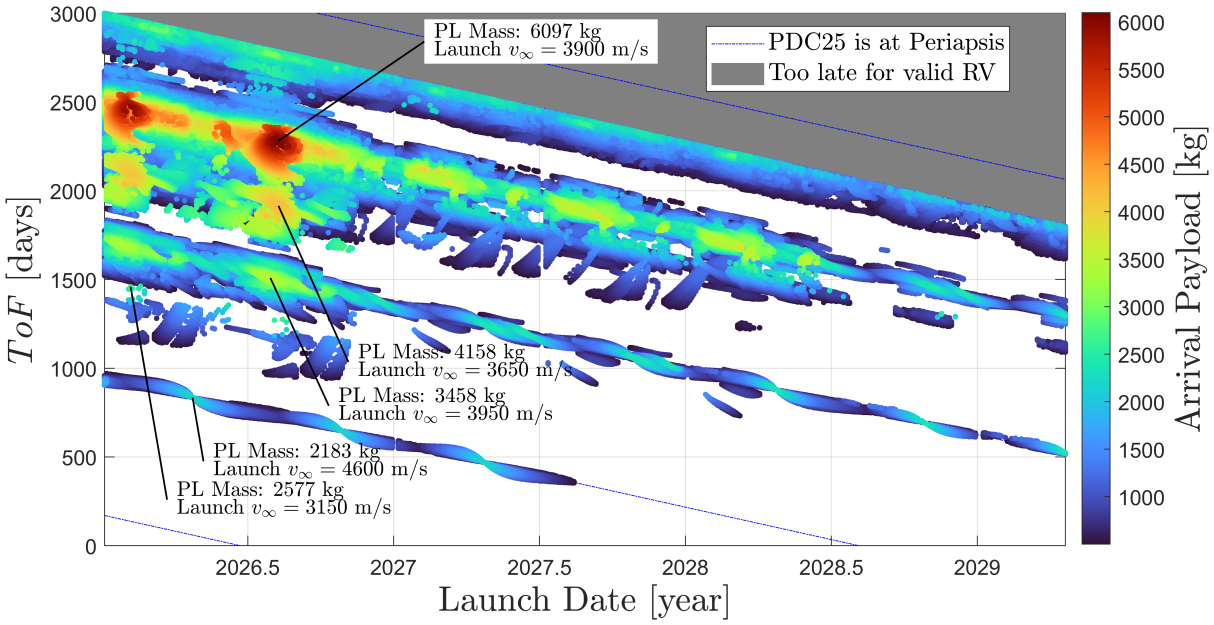

Figure 14: MGA Sequence Independent Payload PCP.

Since the goal of this mission does not depend on where on its orbit PDC25 is found, contrary to the KI, there are good solutions encountering the asteroid far from its periapsis.

Finally Figure 15 shows every trajectory that flies by PDC25 at a relative velocity under 3 km/s. The equivalent Figure 4 corresponding to the direct transfer is much more densely populated. This difference is due to the gravity assist trajectories being limited to a smaller launch energy. One can see that the local minima in Figure 4 require launch velocities around 8 km/s to achieve gentle encounters under 1 km/s. Gravity assists offer the same result at much smaller launch velocities attainable to less powerful vehicles, but in exchange for longer flight times.

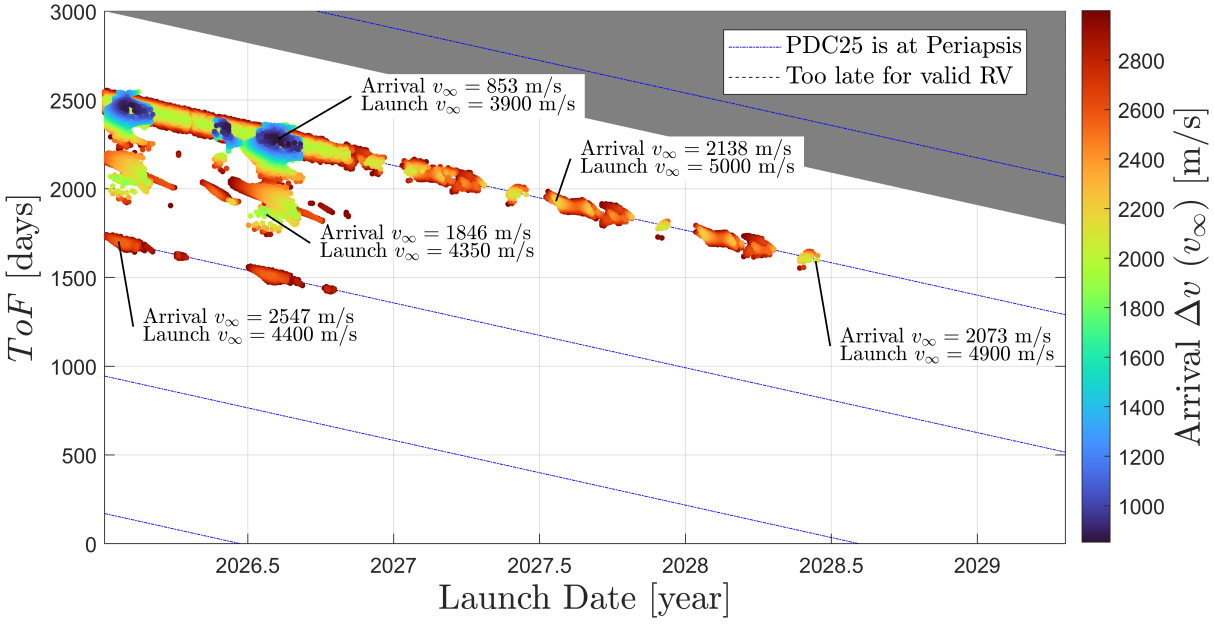

Figure 15: MGA Sequence Independent Payload PCP.

7.2. Best of the best

Figure 16 gives an idea of the ecliptic projection of the best KI and RV trajectories found. When planets are visited more than once consecutively, they are labeled as $+X$, where X is the number of

years between the first visit and each resonant encounter. Numerical data on these trajectories can be found in Tables 3 and 4.

Notably, the two trajectories in Figure 16 are incompatible if the reconnaissance is to happen before the impact. For that reason, several other interesting maxima for asteroid deflection and payload mass have been plotted in Figures 17 and 18. Particularly for Figure 18, the complete knowledge of the solution space allows the imposition of further restrictions that simply require a filtering of the available solutions. Maxima allowing for more than 2 and more than 6 months of decision before the 2030 and 2032 periapsis crossing have been included in Figure 18. These could be paired with deflection candidates in Figure 17. For example, the best deflection available for Figure 16a could be paired with the RV solution in 18b.

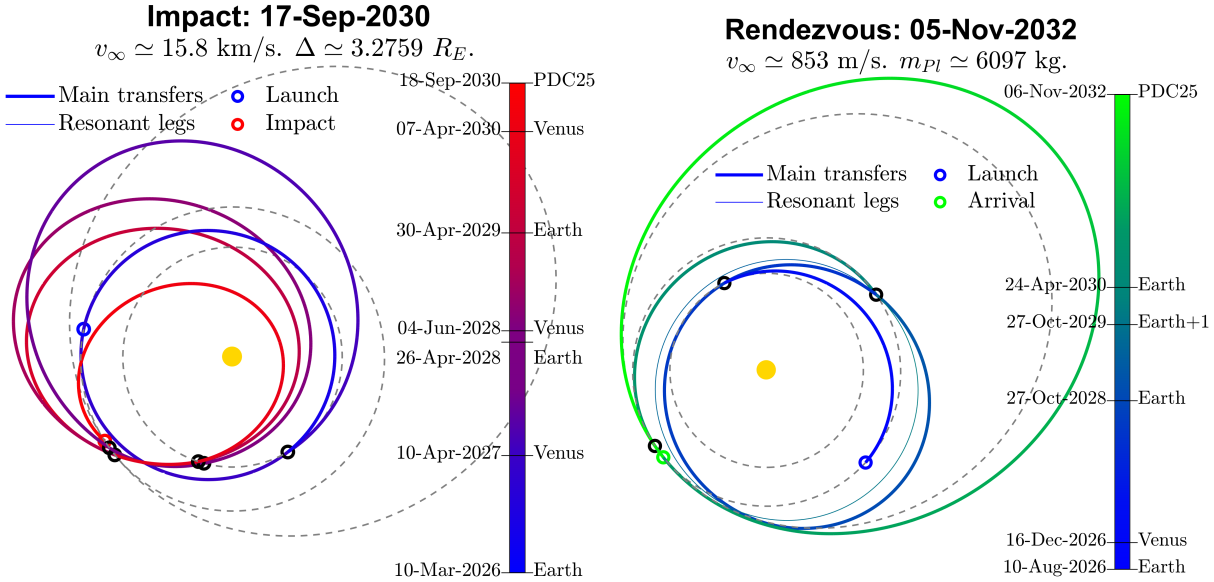

(a) Best KI in the solution space **(b) Best RV in the solution space**

Figure 16

Table 3: Best KI data

Level χ	Body	Epoch t_χ	v_{∞_χ} km/s	Resonance (outgoing)	v_{∞_χ} deflection δ deg.
0	Earth	10-Mar-2026	3.45	–	–
1	Venus	10-Apr-2027	6.29	–	51.71
2	Earth	26-Apr-2028	11.32	–	35.80
3	Venus	04-Jun-2028	17.15	–	13.02
4	Earth	30-Apr-2029	15.40	–	6.07
5	Venus	07-Apr-2030	18.82	–	13.88
6	PDC25	18-Sep-2030	15.80	–	–

Table 4: Best RV data

Level χ	Body	Epoch t_χ	v_{∞_χ} km/s	Resonance (outgoing)	v_{∞_χ} deflection δ deg.
0	Earth	10-Aug-2026	3.90	–	–
1	Venus	16-Dec-2026	5.94	–	51.45
2	Earth	27-Oct-2028	8.77	1 : 1	51.85
	Earth	t_2+ 1 E. year	–	–	44.17
3	Earth	24-Apr-2030	8.66	–	49.15
4	PDC25	06-Nov-2032	0.85	–	–

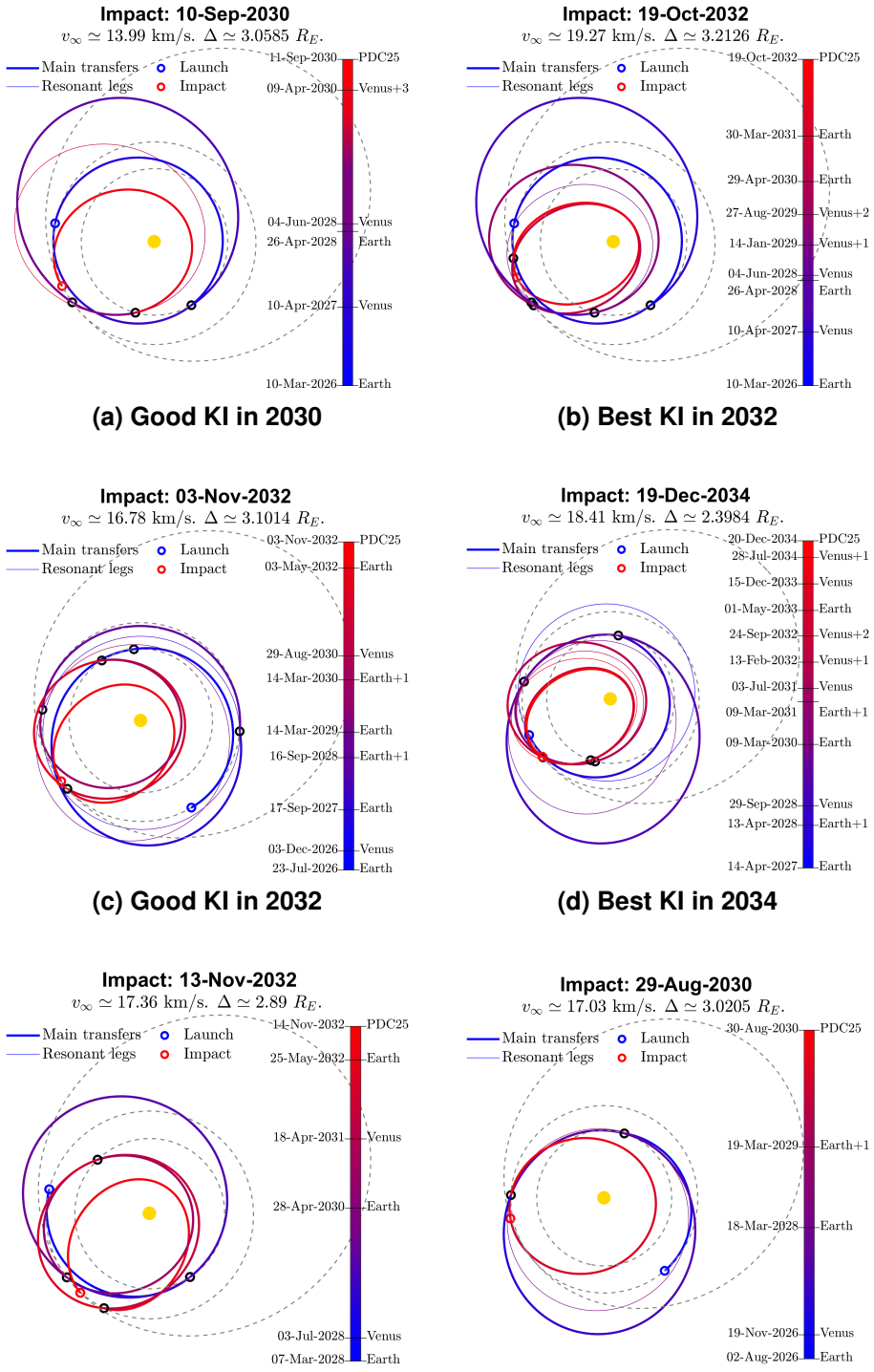

(a) Good KI in 2030 **(b) Best KI in 2032**

(c) Good KI in 2032 **(d) Best KI in 2034**

(e) Backup departure 2028 **(f) Short sequence KI in 2030**

Figure 17: KI Candidates: Numerical data available on Tables 9 to 14

8. Characterization of the Complete Solution Space

This section aims to study the structure of the results obtained in the sequence-independent trajectory search. To that end, Table 5 shows every unique main sequence found in the solution set labeled by the initials of the intermediate flyby bodies.

Within each main sequence instance, there can be many subsequences depending on resonances. For example, the sequence in Figure 17d would be classified as “VEVEV”, although in fact, it includes a larger number of flybys. Although not present in Table 5, “DIRECT” transfers also exist within the solution set. As can be gathered from the algorithm in Figure 12, there is nothing preventing PDC25

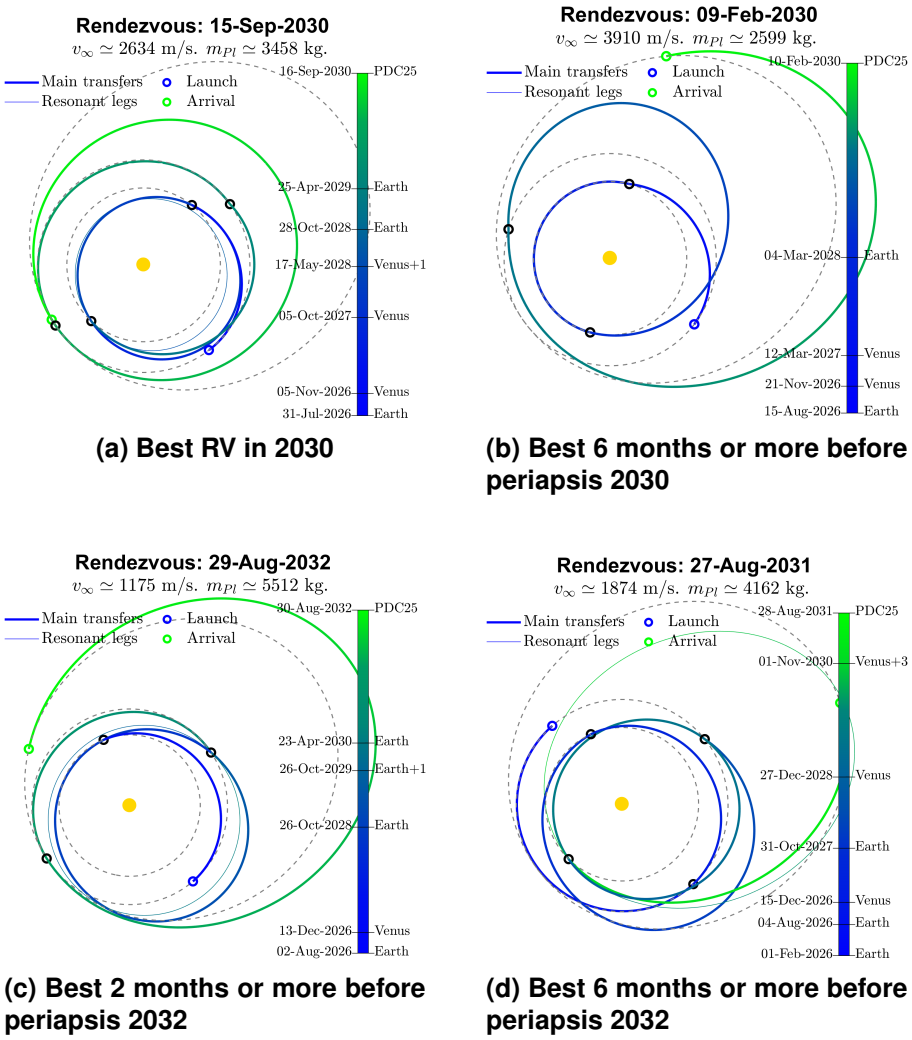

(a) Best RV in 2030

(b) Best 6 months or more before periapsis 2030

(c) Best 2 months or more before periapsis 2032

(d) Best 6 months or more before periapsis 2032

Figure 18: RV Candidates: Numerical data available on Tables 15 to 18

from being a target when $\chi = 0$, meaning that the resulting successful transfers are already complete sequences by themselves and belong to the solution set $\mathcal{S}$.

While many sequences have been found, not all of them are equally good. Considering $\Delta = 1.5$ Earth radii to be the bare minimum required deflection reduces the possible number of sequences to 168, of which 49 have at least one individual solution with $\Delta > 2.5$ and can be considered "very good".

Figures 19 and 20 present a map of all sequences in the "good" and "very good" subset and provide some solid insight on how to build effective MGA trajectories. Each sequence has been plotted according to the number of instances matching it in the solution set $\mathcal{S}$ and the percentage of them achieving good or very good deflection values. Additionally, points have been colored according to the deflection obtained by the best solution for each sequence. Table 6 shows the numerical data used to construct Figure 20.

In general, the longer the sequence, the more solutions available, but the more prone trajectories are to be less effective impactors. This was to be expected, but the more interesting fact is how each particular additional flyby affects the overall sequence in this regard. The most solid formula for a good sequence involves alternating Venus and Earth flybys. For instance, including a single Venus flyby (E →"V"→PDC25) gets $\sim 62.3\%$ of resulting trajectories above $\Delta = 1.5$. A simple alternation like "VEV" results in a lower percentage of good solutions $\sim 44.6\%$, as some will inevitably waste time with little v_∞ gains, but gets a higher best deflection. The trend continues with "VEVEV", with a smaller $\sim 17.2\%$ of solutions being good, but making up for it with the best deflection in the whole solution set.

On the contrary, extending sequences with non-resonant same planet transfers like "EE","VV","EEE" or "VVV" is not a successful strategy. For instance, "EVVE" and "EVEE" not only perform worse than "EVE" in terms of percentage of good trajectories, but also in terms of maximum deflection. It can be

Table 5: All unique main sequences in the solution set. Good: at least 1 solution $\Delta > 1.5$. Very Good: at least 1 solution $\Delta > 2.5$.

MMEEM	MEMVM	VMMEV	VMME	MMEE	MMMEV	MMEME	MMME
MEEMV	VMVEJ	VEMMV	VEVMM	EVEJ	EVEMM	MME	VEMJE
EMEMV	VVMME	MEMV	VMEVM	MMMEE	VEMMM	MMEV	MMMMM
VVMVM	EMMEE	EVEMJ	VMVM	MMEM	VEMEJ	VMVMV	MMMM
EMME	EEVEJ	VVMEM	VEMM	EEMME	EVMVM	MEEMM	EMMEV
MEMEM	VEMJ	VVEMJ	EVMME	MMMEM	VMEM	MMEEV	VEMME
VVMVV	EMMEM	VMVVV	EMMMM	MEVVM	EVMEM	EMEVM	VMVME
MEEVM	M	VM	VEEMM	VMEMV	VVMV	MEMVV	VEMVM
VVM	MMEVE	VMVV	VMVEM	VMEEM	VEVEJ	VEEMJ	MEVM
MMEEE	MEMVE	VMV	EVVM	VME	EMEME	EVVMV	VMEVV
VVMEE	VVVMV	MEVMV	VVEMV	VVME	VEMVV	MEMEV	VMEME
VVVM	EVMVV	EM	VEVVM	MEMEE	VMVVE	EVM	**VMEEE**
MEME	EMEEM	VEEMV	VVVVM	VVMEV	VVMVE	VMEE	VMEEV
EEVVM	MEEM	MEM	EVVVM	VEMV	MEEME	VMEV	VEVM
VEMEM	EVVME	VEEVM	EVMV	MEVME	EMEM	VVVME	MEVEM
VMVEE	VMVE	EVME	**V**	EEVM	VVEVM	EVEMV	VMVEV
VEM	EVEVM	EVMEE	ME	EEM	VV	MEE	MEV
EMEVV	MEEEM	EMEV	EEMEM	EME	EMEEV	EEVMV	VMEVE
EMEE	EVMVE	MEEV	**VEVMV**	EEEVM	MEVV	EVMEV	VEMVE
VVEM	VEEM	E	EEVME	**EV**	VEMEV	EVEM	**VEME**
VEVME	**VEEME**	EEMEV	VEMEE	**VVV**	EMEEE	MEEEV	EEMEE
MEVVV	EVV	**EMEVE**	VVVEM	**VVEME**	VEEEM	VEVEM	**VE**
MEEVV	EEME	EEEM	VVEEM	**MEVEV**	**MEVE**	EVVEM	EEEME
MEEEE	VVVV	EVEEM	MEEVE	MEVEE	**EVEME**	MEEE	MEVVE
VVE	EEVEM	**VEV**	EE	EEV	**VEVV**	**VEE**	**EVVV**
VEEV	VVEV	**EVE**	VEVVV	VEEEV	EEVV	EEEEM	VVEEV
VVEVV	VEEVV	**EVEV**	VVVVV	**VVEE**	**VVVE**	**VEEE**	**EVEVV**
VVVEV	EEEV	**EVEEV**	EVVVV	**EVVE**	**EVEE**	EEE	**VEEEE**
VEVE	**EVVEV**	**VVEEE**	**VEVVE**	**VEVEE**	**VVVEE**	**VVVVE**	**VEVEV**
EEVVV	**EVEEE**	EEVEV	**VEEVE**	EEEVV	**EEVE**	**EVVVE**	**EVVEE**
VVEVE	EEVEE	EEEEV	**EVEVE**	EEVVE	EEEE	**EEEVE**	EEEEE

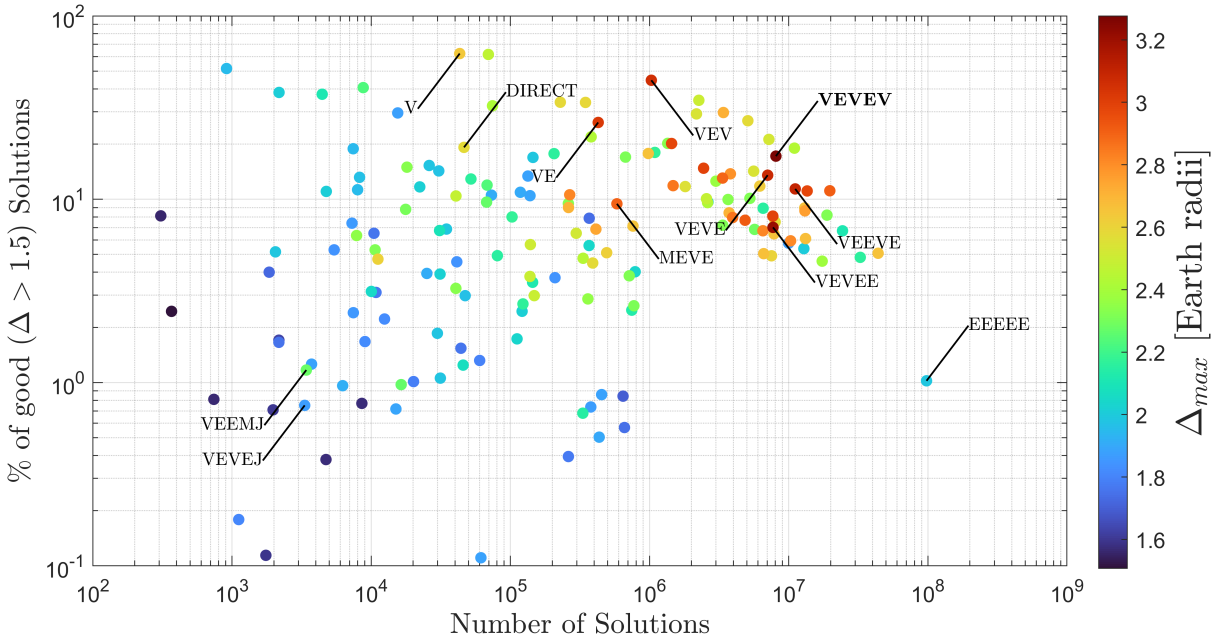

Figure 19: Frequency and percentage of solutions above $\Delta = 1.5$.

seen in Figure 20 that sequences involving many consecutive Venus or Earth flybys are consistently lower in the map, having a smaller proportion of good individual trajectories. In spite of this fact, outliers

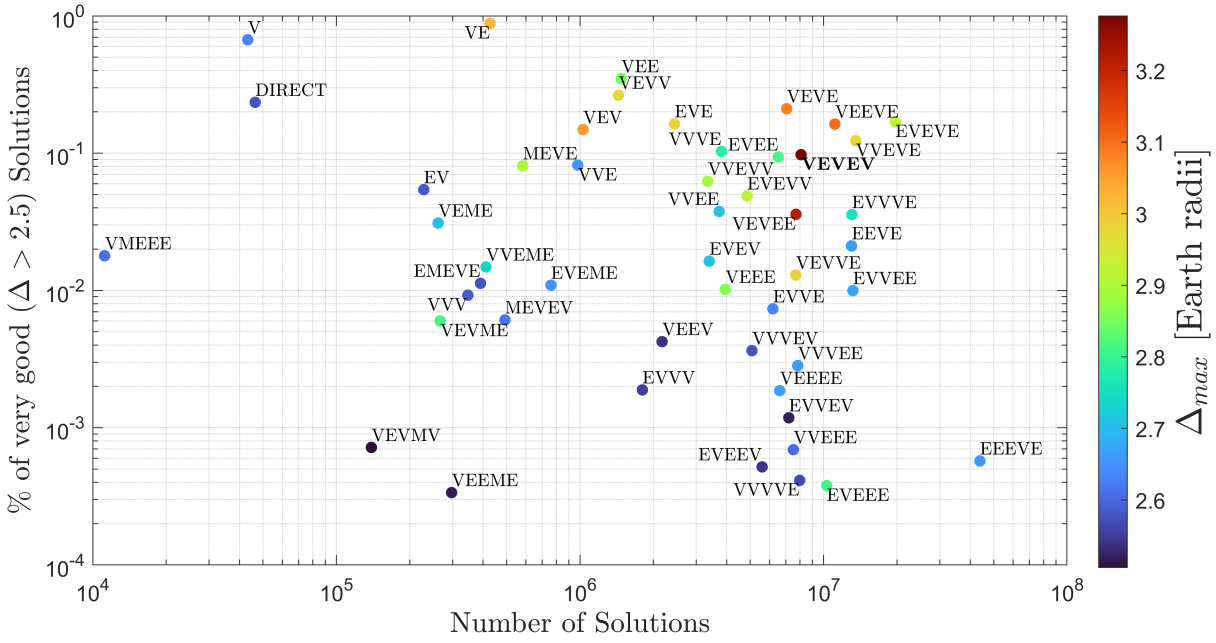

Figure 20: Frequency and percentage of solutions above $\Delta = 2.5$.

do exist, like “VEEVE” and “VEVEE”, outmatching “VEVE” in terms of maximum deflection achieved. Even if consecutive flybys are in general not effective, it is important to notice that most sequences in Figure 20 still improve on the “DIRECT” solution, meaning that even if they require spending time on flybys, they make up for it with a larger impact velocity, which justifies obtaining and looking at them.

Trajectories involving Mars are less promising in general, as Mars offers little $\boldsymbol{v}_\infty$ deflection potential and requires increasing the semi major axis, meaning longer transfer legs and fewer flybys doable in the available flight time. Interestingly, Jupiter-involving sequences do not perform too well either, showing that even if stronger impacts can result from Jupiter swing-bys, not enough so to counteract the effect of the shorter deflection propagation time. Were the time before the impact longer than 17 years, however, the unmatched impact velocity that Jupiter sequences can achieve would undoubtedly result in very interesting alternatives.

Finally, Earth-only sequences, which are strongly present in the MGA solution space, (around $\sim 28\%$ of $\mathcal{S}$ is “EEEEE”) are unsurprisingly very modest in terms of deflection, offering a general disadvantage over the direct transfer, as deflection propagation is lost time is lost with minimal v_∞ gains to compensate.

8.1. Involvement of Venus, Mars and Jupiter in the solution space

Figure 21 highlights different subsections of the complete solution set resulting from the inclusion or avoidance of particular assisting bodies in the sequence. Firstly, Figure 21a shows the part of the solution set corresponding to sequences not passing by the Earth again. A majority of these are ”V^r”, where $r = 1, 2, \ldots, 5$. But anything involving Venus and Mars is also included, along with all $\Delta > 1.5$ direct transfers. The best solution in this subset achieves $\Delta \simeq 2.64$, slightly over the direct transfer but not significantly.

Figure 21b reveals the overwhelming presence of solutions using only Earth and Venus, this subset contains the most interesting extrema that can be seen in Figures 17 and 18. The subset using Mars gravity assists is shown in Figure 21c. As expected, Mars involves longer times of flight in general, with almost no trajectories totaling less than 1500 days. From Table 6 one can gather that the best Mars-involving sequence is “MEVE”, with a maximum deflection of $\Delta \simeq 2.90$ (Figure 22a).

Finally, involving Jupiter requires even longer flight times, as can be seen in Figure 21d. Notably, however, these trajectories impact PDC25 relatively far from the optimal point at perihelion, once again showing how strong Jupiter can be at accelerating the impactor. Even with poor phasing and a short deflection propagation time, these Jupiter solutions are still showing up with $\Delta > 1.5$. The best trajectory (Figure 22b) in this subset corresponds to the “VEEMJ” sequence with $\Delta \simeq 2.28$.

Table 6: Very good sequences: each has at least one solution with $\Delta > 2.5$.

Sequence	Count	of which $\Delta > 2.5$	Δ_{max}	Sequence	Count	of which $\Delta > 2.5$	Δ_{max}
VEVMV	139225	1	2.51	VEEME	297214	1	2.52
VMEEE	11182	2	2.61	VEVME	266834	16	2.81
EVEEV	5594983	29	2.54	MEVEV	492031	30	2.61
VVV	346548	32	2.59	VVVVE	7981005	33	2.57
EVVV	1803722	34	2.55	EVEEE	10307985	39	2.81
EMEVE	390383	44	2.58	VVEEE	7517322	52	2.60
VVEME	411542	61	2.74	VEME	261572	81	2.71
EVEME	760314	83	2.65	EVVEV	7199799	85	2.52
VEEV	2172431	92	2.54	VEEEE	6605915	123	2.66
EV	228443	124	2.58	VVVEV	5082127	185	2.58
VVVEE	7834252	222	2.66	EEEVE	43837022	251	2.65
V	43266	290	2.64	VEEE	3951257	402	2.86
EVVE	6193216	455	2.63	MEVE	582501	471	2.90
EVEV	3392262	554	2.72	VVE	978989	801	2.66
VEVVE	7682194	993	2.99	EVVEE	13195229	1316	2.67
VVEE	3728311	1403	2.71	VEV	1029629	1530	3.06
VVEVV	3344364	2086	2.89	EVEVV	4856266	2369	2.92
EEVE	13023567	2750	2.66	VEVEE	7705767	2764	3.21
VE	427552	3775	3.02	VEVV	1439474	3802	2.97
VVVE	3808032	3926	2.79	EVE	2444413	3995	2.99
EVVVE	13069326	4667	2.76	VEE	1476146	5150	2.85
EVEE	6518813	6122	2.82	VEVEV	8084733	7883	3.28
VEVE	7055342	14868	3.08	VVEVE	13557641	16689	2.98
VEEVE	11128483	18132	3.10	EVEVE	19720917	33341	2.92
DIRECT	46434	109	2.58				

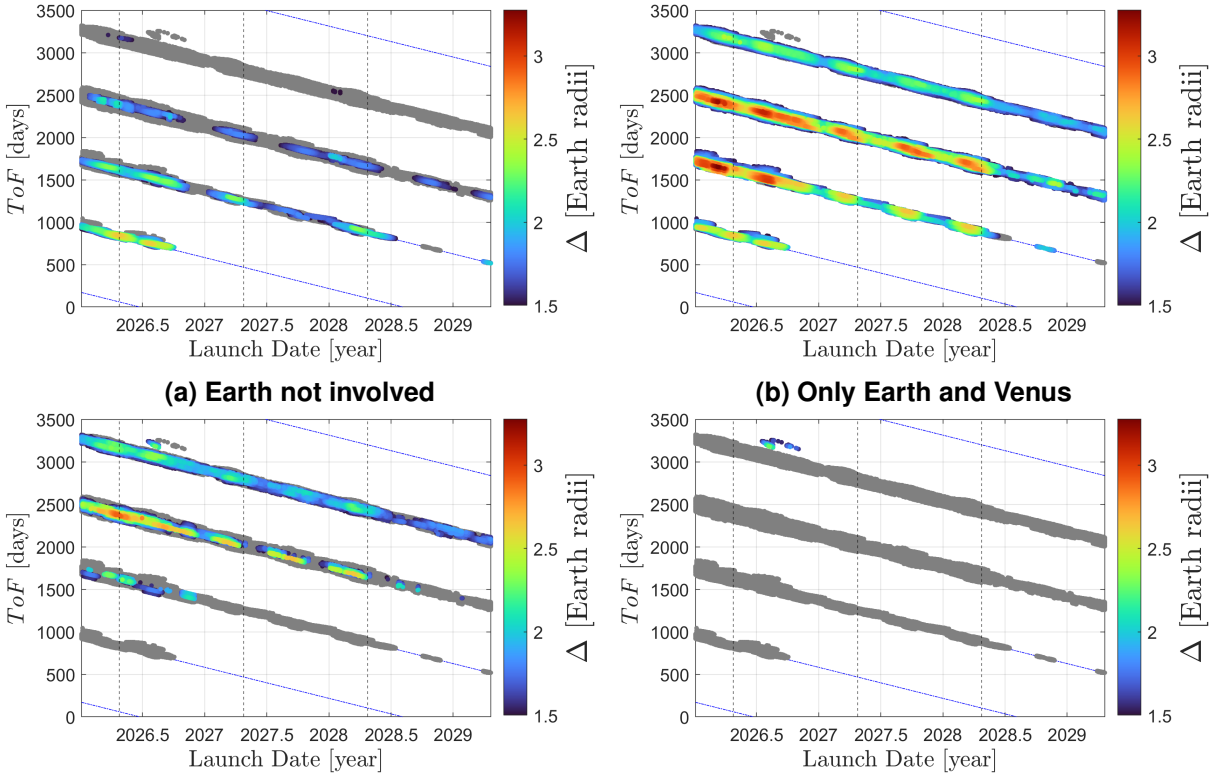

(a) Earth not involved

(b) Only Earth and Venus

(c) Sequences involving Mars

(d) Sequences involving Jupiter

Figure 21

8.2. Effect of sequence length

Figure 23 shows the breakdown of the solution space by sequence length. The more flybys are involved, the longer the trajectories are on average, which can be observed clearly. It also becomes

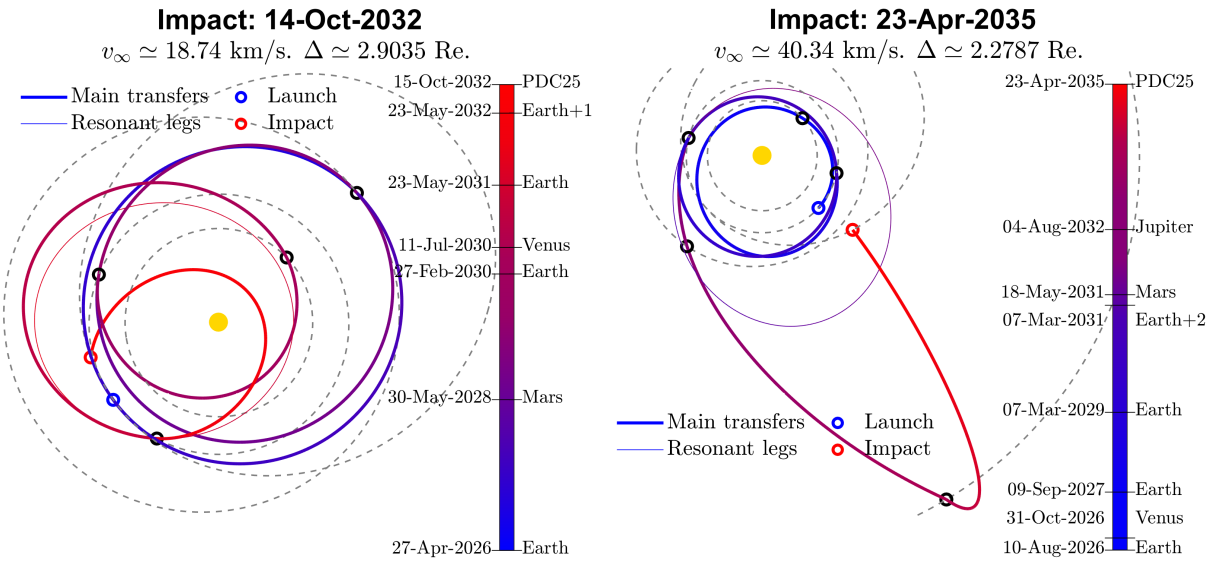

(a) Best impactor involving Mars **(b) Best impactor involving Jupiter**

Figure 22

Table 7: Sequence Data

Level χ	Body	Epoch t_χ	v_{∞_χ} km/s	Resonance (outgoing)	v_{∞_χ} deflection δ deg.
0	Earth	27-Apr-2026	2.90	–	–
1	Mars	30-May-2028	4.23	–	23.71
2	Earth	27-Feb-2030	7.38	–	49.74
3	Venus	11-Jul-2030	11.65	–	29.25
4	Earth	23-May-2031	13.18	1 : 1	22.79
	Earth	t_4+ 1 year	–	–	28.74
5	PDC25	15-Oct-2032	18.73	–	–

Table 8: Sequence Data

Level χ	Body	Epoch t_χ	v_{∞_χ} km/s	Resonance (outgoing)	v_{∞_χ} deflection δ deg.
0	Earth	10-Aug-2026	4.65	–	–
1	Venus	31-Oct-2026	10.37	–	19.70
2	Earth	09-Sep-2027	10.33	–	36.31
3	Earth	07-Mar-2029	10.40	1 : 2	41.66
	Earth	t_3+ 2 years	–	–	41.04
4	Mars	18-May-2031	19.21	–	3.54
5	Jupiter	04-Aug-2032	12.20	–	41.71
6	PDC25	23-Apr-2035	40.34	–	–

apparent that having only one flyby in the main sequence (not counting resonances) does not offer significant improvements over the previously discussed direct transfer maxima. As mentioned, a single flyby of Venus achieves the maximum with $\Delta \simeq 2.64$. Allowing two intermediate flybys results in a 0.4 increase in deflection, with the "VE" sequence providing the best solution at $\Delta \simeq 3.02$. Further lengthening the sequence results in smaller but significant improvements of the top solutions. The trajectories within each increasing length set get worse on average, but the best deflection values do increase, showing that the growth in the number of possibilities outweighs the negative effect of longer flight times. "VEV" features the maximum for the $\chi = 3$ set at $\Delta \simeq 3.06$, and similarly "VEVE" further pushes it to $\Delta \simeq 3.08$ for $\chi = 4$. As already mentioned, at the $\chi = 5$ limit "VEVEV" and "VEVEE" provide the best solutions found with $\Delta \simeq 3.28$ and $\Delta \simeq 3.21$.

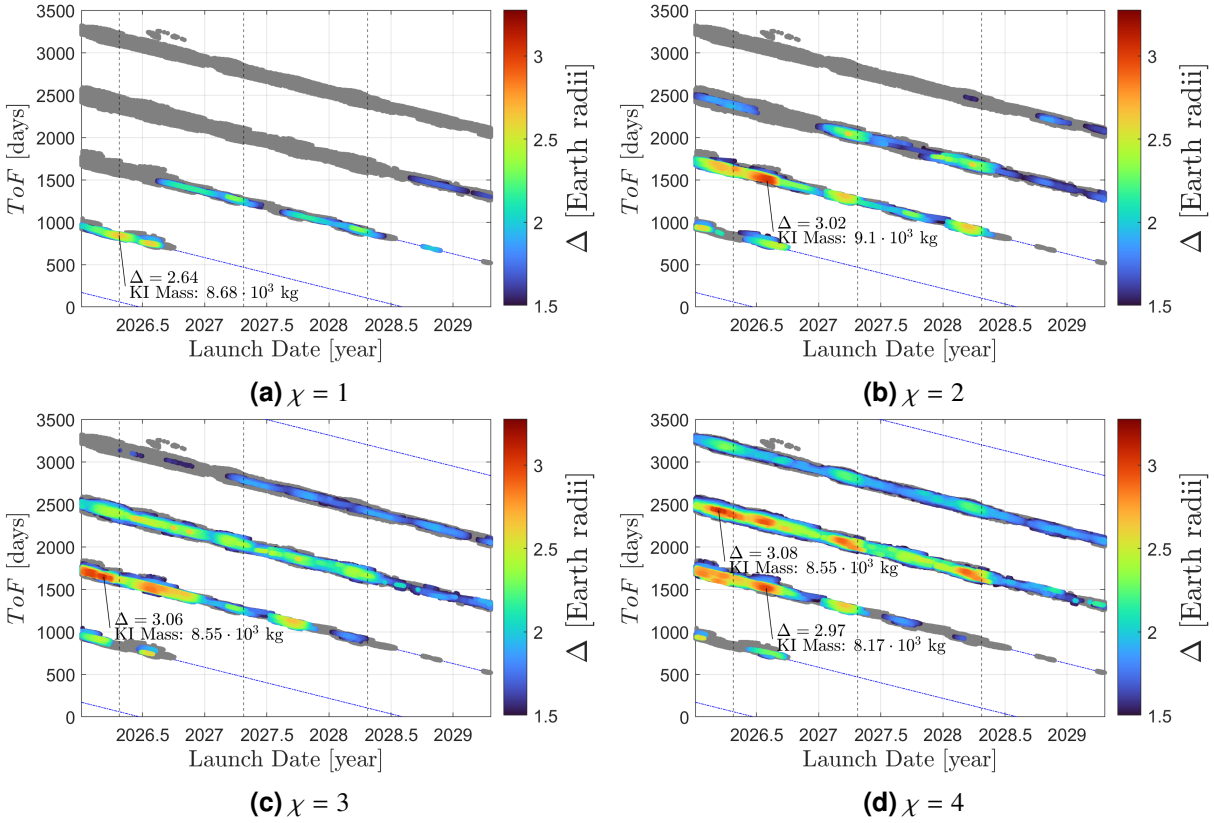

(a) $\chi = 1$ **(b)** $\chi = 2$

(c) $\chi = 3$ **(d)** $\chi = 4$

Figure 23: Subset of the solution space corresponding to different sequence lengths

9. Conclusion

In the context of the hypothetical asteroid threat exercise for the 2025 Planetary Defense Conference, an exhaustive sequence-independent search of multiple gravity assist trajectories to the fictitious asteroid PDC25 has been proposed and conducted with the method published in [1] where the classical C_3 energy-matching main algorithm has been replaced with a new time-matching alternative which avoids the use of a Lambert's Problem solver. The exhaustive trajectory finder has been improved to include odd and even-π resonant legs in the ballistic solutions by solving pathfinding problems in the v_∞-Sphere, resulting in complete knowledge of the solution space, allowing one to select any pair of compatible rendezvous and kinetic impactor trajectories within it at will.

Solving a large grid of initial conditions (departure time and energy) more than 500 million individual trajectories have been obtained and studied. This has allowed the production of MGA pork-chop plots for the achievable deflection of asteroid PDC25 with a kinetic impactor, as well as the identification of local and global optima corresponding to the "VEVEV" sequence achieving $\Delta \simeq 3.28$ Earth radii of deflection. It can also be concluded that to reach PDC25 with similar velocities, direct trajectories need much larger C_3 values at launch than MGA sequences. This results in lower impactor mass and less overall deflection, even if secular propagation works in favor of direct transfers. MGA solutions require longer flight times, but in exchange offer much lighter launch C_3 requirements and thus larger impactor masses. Due to the long time span between the detection of PDC25 and the potential impact with the Earth, this tradeoff is shown to be an effective strategy, with MGA trajectories achieving up to a 27% increase in deflection as well as considerably more flexible launch windows.

For the reconnaissance mission, where the goal is to get the largest payload mass possible, MGA trajectories more than double the total mass that can be taken to PDC25, with respect to direct transfers, also due to the much more affordable launch energies.

The complete characterization of the sequence independent solution space also allows for the identification of the effective sequence building strategies. Although outliers do exist, it has been shown that alternating sequences like "EVEVE" or "VEVEV" result in more effective impactors, also increasing in deflection capability with sequence length, even if the deflection has less time to secularly propagate. As expected, analysis of the planetary involvement in the solution space shows that the Venus-Earth

system is the most effective for this particular problem. Including Mars results in excessively long total flight times, hampering the propagation of the deflection. Finally, although Jupiter can result in impacts at PDC25 at more than 40 km/s through the "VEEMJ" sequence, the shorter propagation time paired with poor phasing of the impact ends up resulting in less effective impactor missions.

10. Appendix 1: Numerical Data for individual trajectories

Table 9: Figure 17a

Level χ	**Body**	**Epoch** t_χ	$v_{\infty,\chi}$ km/s	**Resonance** (outgoing)	$v_{\infty,\chi}$ **deflection** δ deg.
0	Earth	10-Mar-2026	3.45	–	–
1	Venus	10-Apr-2027	6.29	–	51.71
2	Earth	26-Apr-2028	11.32	–	35.80
3	Venus	04-Jun-2028	17.15	2 : 3	11.60
	Venus	t_3+ 3 V. years	–	–	16.95
4	PDC25	11-Sep-2030	13.99	–	–

Table 10: Figure 17b

Level χ	**Body**	**Epoch** t_χ	$v_{\infty,\chi}$ km/s	**Resonance** (outgoing)	$v_{\infty,\chi}$ **deflection** δ deg.
0	Earth	10-Mar-2026	3.45	–	–
1	Venus	10-Apr-2027	6.29	–	51.71
2	Earth	26-Apr-2028	11.32	–	35.80
3	Venus	04-Jun-2028	17.15	1 : 1	3.05
	Venus	t_3+ 1 V. year	–	1 : 1	0.00
	Venus	t_3+ 2 V. years	–	–	8.04
4	Earth	29-Apr-2030	13.03	–	29.79
5	Earth	30-Mar-2031	12.92	–	24.55
6	PDC25	19-Oct-2032	19.27	–	–

Table 11: Figure 17c

Level χ	**Body**	**Epoch** t_χ	$v_{\infty,\chi}$ km/s	**Resonance** (outgoing)	$v_{\infty,\chi}$ **deflection** δ deg.
0	Earth	23-Jul-2026	2.85	–	–
1	Venus	03-Dec-2026	5.04	–	32.12
2	Earth	17-Sep-2027	7.79	1 : 1	59.43
	Earth	t_2+ 1 E. year	–	–	25.48
3	Earth	14-Mar-2029	7.88	1 : 1	58.70
	Earth	t_3+ 1 E. year	–	–	55.97
4	Venus	29-Aug-2030	15.44	–	6.89
5	Earth	03-May-2032	9.90	–	43.82
6	PDC25	03-Nov-2032	16.78	–	–

Acknowledgments

This work was supported by grant TED2021-132099B-C33 funded by the Spanish State Research Agency 10.13039/501100011033. The authors thank the Ministry of Science, Innovation and Universities of Spain for the financial support.

The authors gratefully acknowledge the Universidad Politécnica de Madrid (www.upm.es) for providing computing resources on Magerit Supercomputer.

Table 12: Figure 17d

Level χ	Body	Epoch t_χ	$v_{\infty,\chi}$ km/s	Resonance (outgoing)	$v_{\infty,\chi}$ deflection δ deg.
0	Earth	14-Apr-2027	3.25	$1:1$	0.00
	Earth	t_0+ 1 E. year	–	–	–
1	Venus	29-Sep-2028	6.64	–	63.10
2	Earth	09-Mar-2030	11.16	$1:1$	11.67
	Earth	t_2+ 1 E. year	–	–	31.41
3	Venus	03-Jul-2031	17.99	$1:1$	0.72
	Venus	t_3+ 1 V. year	–	$1:1$	0.00
	Venus	t_3+ 2 V. years	–	–	4.47
4	Earth	01-May-2033	12.62	–	27.67
5	Venus	15-Dec-2033	22.09	$1:1$	6.51
	Venus	t_5+ 1 V. year	–	–	6.69
6	PDC25	20-Dec-2034	18.41	–	–

Table 13: Figure 17e

Level χ	Body	Epoch t_χ	$v_{\infty,\chi}$ km/s	Resonance (outgoing)	$v_{\infty,\chi}$ deflection δ deg.
0	Earth	07-Mar-2028	3.40	–	–
1	Venus	03-Jul-2028	5.81	–	30.24
2	Earth	28-Apr-2030	8.98	–	41.98
3	Venus	18-Apr-2031	15.79	–	6.18
4	Earth	25-May-2032	10.98	–	37.65
5	PDC25	14-Nov-2032	17.36	–	–

Table 14: Figure 17f

Level χ	Body	Epoch t_χ	$v_{\infty,\chi}$ km/s	Resonance (outgoing)	$v_{\infty,\chi}$ deflection δ deg.
0	Earth	02-Aug-2026	3.00	–	–
1	Venus	19-Nov-2026	6.08	–	49.30
2	Earth	18-Mar-2028	9.82	$1:1$	44.93
	Earth	t_2+ 1 E. year	–	–	29.49
3	PDC25	30-Aug-2030	17.03	–	–

Table 15: Figure 18a

Level χ	Body	Epoch t_χ	$v_{\infty,\chi}$ km/s	Resonance (outgoing)	$v_{\infty,\chi}$ deflection δ deg.
0	Earth	31-Jul-2026	3.95	–	–
1	Venus	05-Nov-2026	8.59	–	12.11
2	Venus	05-Oct-2027	8.59	$1:1$	48.35
	Venus	t_2+ 1 V. year	–	–	19.65
3	Earth	28-Oct-2028	5.98	–	50.10
4	Earth	25-Apr-2029	5.90	–	30.40
5	PDC25	16-Sep-2030	2.63	–	–

References

[1] M. Gavira-Aladro, C. Bombardelli, Lambert-Free Solution of Multiple-Gravity-Assist Optimization Problem, Journal of Guidance, Control, and Dynamics 47 (2024) 1822–1838.

[2] J. Roa, A. E. Petropoulos, P. W. Chodas, Characterization and deflection missions of the fictitious asteroid 2019 PDC, 2019.

[3] C. Bombardelli, D. Amato, J. L. Cano, Mission analysis for the ion beam deflection of fictitious asteroid 2015 pdc, Acta Astronautica 118 (2016) 296–307.

[4] S. Williams, Automated design of multiple encounter gravity-assist trajectories (1990). M. S. Thesis, School of Aeronautics and Astronautics, Purdue Univ., West Lafayette, IN.

Table 16: Figure 18b

Level χ	Body	Epoch t_χ	v_{∞_χ} km/s	Resonance (outgoing)	v_{∞_χ} deflection δ deg.
0	Earth	15-Aug-2026	3.20	–	–
1	Venus	21-Nov-2026	6.06	–	70.73
2	Venus	12-Mar-2027	6.02	–	71.49
3	Earth	04-Mar-2028	10.68	–	37.55
4	PDC25	10-Feb-2030	3.91	–	–

Table 17: Figure 18c

Level χ	Body	Epoch t_χ	v_{∞_χ} km/s	Resonance (outgoing)	v_{∞_χ} deflection δ deg.
0	Earth	02-Aug-2026	3.90	–	–
1	Venus	13-Dec-2026	6.24	–	51.89
2	Earth	26-Oct-2028	8.86	$1:1$	51.22
	Earth	t_2+ 1 E. year	–	–	44.08
3	Earth	23-Apr-2030	8.76	–	48.18
4	PDC25	30-Aug-2032	1.17	–	–

Table 18: Figure 18d

Level χ	Body	Epoch t_χ	v_{∞_χ} km/s	Resonance (outgoing)	v_{∞_χ} deflection δ deg.
0	Earth	01-Feb-2026	4.25	–	–
1	Earth	04-Aug-2026	4.13	–	36.41
2	Venus	15-Dec-2026	6.48	–	56.42
3	Earth	31-Oct-2027	9.20	–	47.97
4	Venus	27-Dec-2028	12.10	$1:3$	30.00
	Venus	t_4+ 3 V. years	–	–	9.24
5	PDC25	28-Aug-2031	1.87	–	–

[5] J. M. Longuski, S. N. Williams, Automated design of gravity-assist trajectories to mars and the outer planets, Celestial Mechanics and Dynamical Astronomy 52 (1991) 207–220.

[6] D. Lantukh, R. Russell, Automated inclusion of n-pi transfers in gravity-assist flyby tour design, in: Proceedings of the AIAA/AAS Astrodynamics Specialist Conference, Minneapolis, MN. 2012.

[7] C. Bombardelli, Analytical formulation of impulsive collision avoidance dynamics, Celestial Mechanics and Dynamical Astronomy 118 (2014) 99–114.

[8] J. Hernando-Ayuso, D. Amato, C. Bombardelli, Last-minute semi-analytical asteroid deflection by nuclear explosion, in: Proceedings of the 2017 Planetary Defense Conference. International Academy of Astronautics. Tokyo, Japan.

[9] N. Melamed, NASA NEO Deflection Application: Current Capabilities and Limitations, Springer International Publishing, pp. 123–138.

[10] T. J. Ahrens, A. W. Harris, Deflection and fragmentation of near-earth asteroids, Nature 360 (1992) 429–433.

[11] M. Bruck Syal, J. Michael Owen, P. L. Miller, Deflection by kinetic impact: Sensitivity to asteroid properties, Icarus 269 (2016) 50–61.

[12] A. Cheng, P. Michel, M. Jutzi, A. Rivkin, A. Stickle, O. Barnouin, C. Ernst, J. Atchison, P. Pravec, D. Richardson, Asteroid impact & deflection assessment mission: Kinetic impactor, Planetary and Space Science 121 (2016) 27–35.

[13] N. Arora, R. P. Russell, A fast and robust multiple revolution lambert algorithm using a cosine transformation, Advances in the Astronautical Sciences 150 (2014) 411–430.

[14] D. Myatt, V. Becerra, S. Nasuto, J. Bishop, Advanced global optimisation tools for mission analysis and design, Ariadna Final Report (2004).